Large-eddy simulation of magnetohydrodynamics and heat transfer in annular pipe liquid metal flow

Fico, Francesco; Langella, Ivan; Xia, Hao

DOI
10.1063/5.0143687

Publication date
2023

Document Version
Final published version

Published in
Physics of Fluids

RESEARCH ARTICLE | MAY 01 2023

Large-eddy simulation of magnetohydrodynamics and heat transfer in annular pipe liquid metal flow

Francesco Fico ; Ivan Langella ; Hao Xia (夏浩)

Physics of Fluids 35, 055106 (2023)
https://doi.org/10.1063/5.0143687

Physics of Fluids ARTICLE scitation.org/journal/phf

Large-eddy simulation of magnetohydrodynamics and heat transfer in annular pipe liquid metal flow

Cite as: Phys. Fluids **35**, 055106 (2023); doi: 10.1063/5.0143687
Submitted: 25 January 2023 · Accepted: 9 April 2023 ·
Published Online: 1 May 2023

View Online Export Citation CrossMark

Francesco Fico,[1,a)] Ivan Langella,[2] and Hao Xia (夏浩)[1]

AFFILIATIONS

[1]Aeronautical and Automotive Engineering, Loughborough University, Loughborough, United Kingdom
[2]Aerospace Engineering, Flight Performance and Propulsion, TU Delft, Delft, The Netherlands

[a)]Author to whom correspondence should be addressed: f.fico@lboro.ac.uk

ABSTRACT

Turbulent structures in a concentric annular pipe within a uniform transverse magnetic field are examined for a liquid metal flow. Large-eddy simulations are performed to study the effect of magnetic field on turbulence suppression and heat transfer within this geometry. At the characteristic Prandtl number of liquid metals, the smallest scales based on temperature fluctuations are much larger than those of the velocity, which allows to resolve all the temperature scales with sufficient accuracy. The calculations are run at Reynolds number 8900 for three different Hartmann numbers, $Ha = 40, 60, 120$. The comparison with available direct numerical simulation data shows encouraging agreement. The main findings of this work show a circumferential dependency of the flow characteristics on the local orientation of the magnetic field, with increased anisotropy observed at all Hartmann numbers studied. Anisotropic effects of the magnetic field are predominant for $Ha = 60$ and $Ha = 120$ causing turbulence to deviate from its conventional state. At these Hartmann numbers, a partial redistribution of the turbulent kinetic energy from the axial and radial components to the azimuthal component is observed. This effect, observed here for the first time, appears to be related to the appearance of coexisting quasi two-dimensional (2D) and three-dimensional (3D) turbulence states. Moreover, large skin friction increments are also observed at $Ha = 60$ and $Ha = 120$, while coherent structures stretching and streak suppression are found for all three Hartmann numbers.

I. INTRODUCTION

The turbulent flow through concentric annuli has many relevant engineering applications such as heat exchangers, gas-turbines, and fluid cooled nuclear reactors. Commonly in annuli flows, due to the different curvature of the outer (concave) and inner (convex) walls, the distribution of mean quantities is asymmetric, and the transport of momentum and energy is affected accordingly.[1] Over the past decades, various experimental[1–4] and direct numerical simulation (DNS) studies were performed to understand circular pipe flows and structures. Chung *et al.*,[5] Boersma and Breugem,[6] and Bagheri *et al.*[7] conducted DNS studies of turbulent concentric annular flows at various Reynolds numbers. They investigated the effect of transverse curvature on turbulent statistics by comparing the results of two radius ratios and showing that turbulent intensities and Reynolds shear stresses of the inner wall were smaller than those of the outer wall, i.e., the inner wall supplies relatively less turbulent kinetic energy than the outer wall to the same volume. Chung and Sung[8] and Bagheri and Wang[9] extended their DNS study to also include forced turbulent heat transfer under a constant wall heat flux ratio, for $Pr = 0.71$. They showed the sensitivity of the thermal boundary layer thickness to the radius ratio and found that thermal quantity's statistics near the outer wall were larger than those for the inner wall.

All the previous cited studies focused on fluid with Prandlt number of about $Pr \sim 1$. However, in application with large heat loads, non-convectional fluids like liquid metals have been proposed as cooling fluids.[10–12] Liquid metals are characterized by very small Prandtl numbers due to their very large molecular conductivity. This makes them able to exchange energy more efficiently and across smaller surfaces than conventional fluids. Therefore, they are very appealing when the dimension and weight of the heat exchange devices is limited or when high thermal loads are present. In the nuclear energy generation field, liquid metals are envisaged as the primary coolant fluid in

different reactor designs, such as the lead fast reactor (LFR) and the sodium fast reactor (SFR).[12] For nuclear fusion reactors, their application spans from cooling/breeding blanket to divertor of Tokamak-like type fusion nuclear power plants. The physical mechanism of heat transfer to liquid metals, however, significantly differs from that of conventional coolants. Using numerical simulations of heat transfer in liquid metal conditions, Grotzbach[13] showed that the contribution of the molecular thermal conduction to the total heat transfer is much higher for liquid metals than for order one and higher Prandtl number fluids. At the typical Prandtl number of liquid metals, the smallest temperature scales are much larger than the corresponding velocity scales. This allows to perform, with the same mesh resolution of a large-eddy simulation (LES) quality for the velocity field, a *thermal* DNS for the temperature field.[14–17] Marocco and Garita[18] used this combined LES thermal-DNS strategy to evaluate forced and mixed convection in a concentric annulus for liquid metal flows. They noted that the circumferential mesh resolution strongly affects the accuracy of the results and that turbulent heat fluxes were small compared to molecular transport.

Another important property is that liquid metals respond to magnetic effect. When a magnetic field ($\mathbf{B}_0$) is applied to a conductive moving fluid, it induces a current density ($\mathbf{J}$), and the interaction of this current with the magnetic field generates a Lorentz force ℓ_F, defined (per unit volume) as

$$\ell_F = \frac{1}{\rho}(\mathbf{J} \times \mathbf{B}_0). \tag{1}$$

The Lorentz force interacts with the flow and alters the velocity field. In turbulent flows, the effect is even more relevant, as the magnetic field can alter the structure of the turbulence and in some cases can laminarize the flow.[19,20] Consequently, the mixing phenomena and heat transfer characteristics in turbulent flows subjected to a magnetic field can significantly differ from those without a magnetic field. The magnetic interaction is ruled by the Hartmann (*Ha*) number and the *Re*/*Ha* ratio. The Hartmann number represents the ratio between electromagnetic and viscous forces, while the *Re*/*Ha* ratio provides a measure of the relation between inertia and electromagnetic force. Many studies have investigated magnetohydrodynamic (MHD) turbulence. The main findings of these studies can be summarized as follows:

(i) Turbulence suppression,[20–26] characterized as the anisotropic suppression of the Reynolds stress tensor components by the magnetic field;
(ii) Enlargement of the turbulent coherent structures,[23,27–30] which has been observed in both near wall streaks and streamwise vortices;
(iii) Existence of different flow regimes[23,31–34] depending on relative strength of inertia and electromagnetic force, i.e., the *Re*/*Ha* ratio.

Turbulence suppression was first observed in the pioneer experiment of Hartmann and Lazarus,[21] which studied the effect of a homogeneous magnetic field on mercury within a rectangular section duct. Since then, numerous works were performed to shed light on the mechanism behind turbulence suppression.[27,28] Mostly, simple flow cases were considered, as, channel,[23,25,30,35,36] duct,[29,37,38] and pipe[22,24] flows. Furthermore, isotropic turbulence decay was also studied.[26,31] In general, the above studies indicated preferential suppression of velocity fluctuations whose direction was parallel to the direction of the magnetic field. On the other hand, flow turbulent coherent structures stretching was shown by various studies. Krasnov *et al.*[25] performed DNS of channel flow within a uniform spanwise magnetic field, showing increment of the turbulence structure size in both streamwise and spanwise directions. Moreover, Rasam and Pouransari[39] investigated a channel flow within a uniform streamwise magnetic field, finding a substantial elongation of flow structures in the streamwise direction, and that the streaks spacing increased linearly with increasing Hartmann number. Finally, the existence of different flow regimes and the presence of turbulence special states were also observed. In particular, depending on the *Re*/*Ha* ratio, the flow field can be found in a special turbulent state, referred to as quasi two-dimensional (Q2D)[40,41] turbulence. The laminar-turbulent transition in MHD ducts and pipes was investigated by Zikanov *et al.*,[42] finding that in transversal magnetic field, the critical *Re*/*Ha* values for transition from laminar to turbulent flow in the Hartmann boundary are bounded to $200 < Re/Ha < 400$. Smolentsev *et al.*[43] presented a *Ha*–*Re* diagram to identify the flow regime for non-conducting straight rectangular duct. These authors suggested that quasi 2D states turbulence states are found in the range $65\sqrt{Ha} < Re < 200Ha$.

Despite this extensive number of studies of MHD turbulence, only a few have addressed pipe-like geometries, and to the best of the authors' knowledge, no magnetic effect studies exist on annulus geometries. Compared to channel and duct geometries, the presence of circular walls imposes an angular dependency of flow characteristics with the magnetic field orientation. Moreover, the different curvature of convex and concave walls, and the consequent asymmetry of the flow statistics, leads to a not straightforward turbulence–magnetic field interaction, not observable in pipe flows, which can reveal new insight on the MHD turbulence. Annuli flow within magnetic conditioning, also finds various engineering applications, such as solution in nuclear fusion reactor blanket design,[34] in thermal management cooling system for computer chips,[44] and in nano fluid metallurgy processes.[45]

In this paper, well-resolved LES is performed for a turbulent annular flow with a transverse magnetic field. The objectives of this study are to characterize the turbulence suppression, to reveal the destruction mechanism of turbulence, and respective effects on heat transfer characteristics in this type of geometry. The analysis reveals different levels of the Reynolds stress tensor components suppression by varying the *Re*/*Ha* ratio, and increased anisotropy, leading to coexistence of quasi 2D and 3D turbulence states depending on the circumferential location (respectively oriented at 0° and 90° from the magnetic field), in contrast with other studies, where this feature is not observed. Moreover, at low *Re*/*Ha*, the alternation of quasi-2D and 3D turbulence states seems related to the partial redistribution of turbulent kinetic energy from the axial and radial components to the azimuthal component.

The rest of this paper is organized as follows: in Sec. II, the test cases and the numerical algorithm for solving the governing equations are described. In Sec. III, the LES results with no magnetic field effect are first compared with available DNS results. The turbulence suppression mechanism is then analyzed for different magnetic field intensities. Here, two-point correlations and energy spectra are used to identify the turbulent coherent structures at the walls, while the anisotropic invariant map is used to characterize anisotropic effects of the magnetic field. Finally, concluding remarks are summarized in Sec. IV.

II. GOVERNING EQUATIONS AND NUMERICAL METHODS

An incompressible, electrically conductive, Newtonian fluid under uniform heat fluxes and uniform and static magnetic field in a concentric annulus is considered. Figure 1 shows a schematic diagram of the annulus geometrical characteristics. Here, x, r, and θ represent the axial, radial, and azimuthal coordinates, respectively. The Reynolds number based on the bulk velocity U_b and the hydraulic diameter $D_h = 2(R_o - R_i)$ is $Re_{D_h} = 8900$ and the Prandtl number is Pr = 0.026; R_o, R_i are, respectively, outer and inner radius of the annulus, and $R_i/R_o = 0.5$ is the radius ratio. The computational length in the axial direction is $L_x = 25\delta$, with $\delta = (R_o - R_i)/2$ being half of the distance between the two walls. The fluid properties are assumed to be constant and computed at fixed temperature based on experimental data.[46] Continuity, momentum, and energy equations of the incompressible MHD flow at low magnetic Reynolds number (Re_m) are, in Einstein's notation

$$\frac{\partial \bar{u}_i}{\partial x_i} = 0, \tag{2}$$

$$\frac{\partial \bar{u}_i}{\partial t} + \frac{\partial}{\partial x_j}(\bar{u}_i \bar{u}_j) = -\frac{1}{\rho}\frac{\partial \bar{p}}{\partial x_i} - \frac{\partial \tau_{ij}^{sgs}}{\partial x_j} + \nu \frac{\partial \bar{u}_i{}^2}{\partial x_j \partial x_j} + \ell_{F_i}, \tag{3}$$

$$\frac{\partial \bar{\Theta}}{\partial t} + \bar{u}_j \frac{\partial \bar{\bar{\Theta}}}{\partial x_j} = \bar{u}_x \frac{\partial \langle T_w \rangle}{\partial x} + \frac{\partial}{\partial x_j}\left(\alpha \frac{\partial \bar{\Theta}}{\partial x_j}\right), \tag{4}$$

where $(\bar{})$ indicates the spatial filtering, and u_i, p, ρ, and α represent, respectively, velocity vector component, pressure, density, and thermal diffusivity. The velocity vector components, $\mathbf{u}(u_x, u_r, u_\theta)$, are expressed, respectively, in axial, radial, and azimuthal directions. The term $\ell_F = (1/\rho)\bar{\mathbf{J}} \times \mathbf{B}_0$ is the Lorentz force, where $\mathbf{J}$ is the electric current density and $\mathbf{B}_0$ is the imposed magnetic field, oriented at $\theta = 0$, as shown in Fig. 1. Two uniform and equal in magnitude heat fluxes q are applied at the walls. Periodic boundary conditions are applied in the axial (streamwise) direction. Due to these boundary conditions, the temperature T, treated as a passive scalar, grows in the streamwise direction. In order to be able to assign periodic boundary conditions, the modified temperature $\Theta_b = T - \langle T_b \rangle$ is then introduced, whose transport equation is shown in Eq. (4). The first term on the right-hand side of this equation is defined as the constant mean axial wall temperature gradient for constant heat flux condition. Because of the uniform heat load, the time and section averaged temperature increases linearly in the streamwise direction, i.e.,

$$\frac{\partial \langle T \rangle}{\partial x} = \frac{\partial \langle T_b \rangle}{\partial x} = \frac{\partial \langle T_w \rangle}{\partial x} \approx const, \tag{5}$$

where $\langle T_b \rangle$ and $\langle T_w \rangle$ are the local mean peripheral bulk and wall temperature, respectively, at a given streamwise location. The latter is computed following Patankar *et al.*[47] as

$$\frac{\partial \langle T_w \rangle}{\partial x} = \frac{2(q_{w_o} R_o + q_{w_i} R_i)}{\rho c_p U_b (R_o^2 - R_i^2)}, \tag{6}$$

where U_b is the bulk velocity and c_p is the specific heat coefficient at constant pressure. The modified temperature so defined does not grow in the streamwise direction for a fully developed flow. Different applications of this methodology can be found in various works.[8,9,48] Under the condition of low-Reynolds magnetic number (Re_m), the induced magnetic field $\mathbf{B}_i$ is small in comparison to the imposed one;[49] hence, $\mathbf{B}_0$ and $\mathbf{u}$ are not coupled. Thus, the magnetic field affects the velocity field, and not vice versa. In this condition, the induction-less formulation can be used, where the electric density current is computed using the Ohm's law [Eq. (7)] and charge conservation [Eq. (8)] equations

$$\bar{J}_i = \sigma\left(-\frac{\partial \bar{\phi}}{\partial x_i} + \epsilon_{ijk} \bar{u}_j B_{0_k}\right), \tag{7}$$

$$\frac{\partial \bar{J}_i}{\partial x_i} = 0, \tag{8}$$

where ϕ is the electric potential, σ is the electric conductivity of the fluid, and ϵ_{ijk} is the Levi–Civita tensor (alternating unit tensor). Combining Eqs. (7) and (8), one obtains the Poisson equation for the electric potential

$$\frac{\partial^2 \bar{\phi}}{\partial x_i^2} = \frac{\partial}{\partial x_i}(\epsilon_{ijk} \bar{u}_j B_{0_k}). \tag{9}$$

The walls are considered electrically insulated so that a zero-wall normal current density is imposed

$$J_n|_{wall} = -\left.\frac{\partial \phi}{\partial n}\right|_{wall} = 0$$

with n indicating the normal direction to the wall. No-slip boundary conditions are enforced at the annulus walls for the velocity field. The subgrid-scale (SGS) stress tensor, τ_{ij}^{sgs}, appears in Eq. (3) due to the filtering operation and is defined as

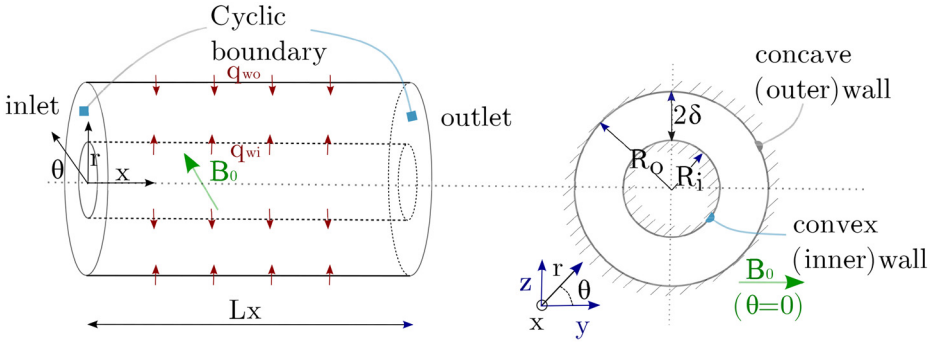

FIG. 1. Concentric annulus geometry. The magnetic field is uniform and oriented at $\theta = 0$ direction. Uniform heat fluxes are applied at the walls. The flow is moved by body force in the positive x direction.

TABLE I. Geometrical, physical, and mesh values. Mesh grid spacing values normalized with mean value of friction velocity u_τ.

Data		Mesh	
Re_{D_h}	8900	$N_x\, N_r\, N_\theta$	(260, 80, 520)
Pr	0.026	$\Delta r^+_{\min}$	0.2
Ha	0, 40, 60, 120	$\Delta r^+_{\max}$	5.3
δ	$(R_o - R_i)/2$	$R_i \Delta\theta^+$	3.6
L_x	25δ	$R_o \Delta\theta^+$	7.2
R_i/R_o	0.5	Δx^+	14

$$\tau^{sgs}_{ij} = \tau_{ij} - \frac{1}{3}\tau_{kk}\delta_{ij}, \quad \tau_{ij} = u_i u_j - \bar{u}_i \bar{u}_j, \tag{10}$$

where δ_{ij} is the Kronecker delta. The SGS stresses are evaluated with wall-adapting local eddy-viscosity (WALE) model[50] as

$$\tau^{sgs}_{ij} = -2\,\nu_{sgs}\,\bar{S}_{ij}, \tag{11}$$

where $\bar{S}_{ij}$ is the resolved strain rate tensor and ν_{sgs} is the SGS viscosity, expressed as

$$\nu_{sgs} = (C_w \Delta)^2 \frac{(\mathcal{S}^d_{ij}\mathcal{S}^d_{ij})^{3/2}}{(\bar{S}_{ij}\bar{S}_{ij})^{5/2} + (\mathcal{S}^d_{ij}\mathcal{S}^d_{ij})^{5/4}}, \tag{12}$$

$$\mathcal{S}^d_{ij} = \frac{1}{2}(\bar{g}^2_{ij} + \bar{g}^2_{ji}) - \frac{1}{3}\delta_{ij}\bar{g}^2_{kk}, \tag{13}$$

$$\bar{g}_{ij} = \frac{\partial \bar{u}_i}{\partial x_j}. \tag{14}$$

In the above, Δ is the cube root of the local cell volume, $C_w = 0.325$ is the model constant, $\bar{g}_{ij}$ is the resolved velocity gradient tensor, and $\mathcal{S}^d_{ij}$ is the traceless symmetric part of the square of $\bar{g}_{ij}$. As mentioned in Sec. I, at very low Prandlt numbers, there is no need for an SGS heat flux model because the grid is sufficiently fine to resolve all temperature scales. Note that summation convection over repeated indices is used in the equations above.

The simulations are carried out with an in-house version of the open source code OpenFOAM,[51] which is modified to include the inductionless approach. The pressure–velocity coupling is solved using PIMPLE methodology that is a combination of pressure-implicit with splitting of operators[52] (PISO) and semi-implicit method for pressure linked equations[53] (SIMPLE) methodologies. The electric potential is computed using Eq. (9), and the electric current is estimated using a conservative interpolation following Ni *et al.*[54] approach. The discretized equations are integrated in time with backward second order implicit scheme. The spatial discretization is made through pure central differences. The overall accuracy in both time and space is then second order. The mesh is uniform in the azimuthal and axial directions, while a non-uniform spacing is used in the radial direction, with the control volumes clustered toward the walls. The stretching factor, expressed as the ratio between the largest and the smallest cell width, is 25. Table I summarizes the geometrical, physical, and mesh characteristics, where N_x, N_r, and N_θ are the number of cells in the axial, radial, and azimuthal directions, while Δr^+, $R_{i/o}\,\Delta\theta^+$, and Δx^+ are the grid spacing in the radial, azimuthal, and longitudinal directions. The temporal averages, denoted by $\langle\cdot\rangle$, are collected over a computational time of 1000 t^*, where $t^* = D_h/U_b$ is the characteristic time. Wall coordinates, represented using the subscript $(^+)$, are normalized using the kinematic viscosity ν and the friction velocity $u_\tau = \sqrt{\tau_w/\rho}$, where τ_w is the wall shear stress. The friction velocity is defined, respectively, for convex (inner) and concave walls (outer). When using global coordinates (normalized by the half-walls distance δ), the mean value of u_τ is taken. The radial coordinate r from inner to outer wall is defined as $r = r^* - R_i$, where r^* is the generic radial coordinate with origin at the center of the annulus.

III. RESULTS AND DISCUSSION

A. Validation of velocity and temperature field without magnetic field

To ascertain the reliability and accuracy of the present numerical simulations, the LES data are first validated against DNS data[5,7–9] and further LES data.[16] Figure 2 compares the averaged velocity profile

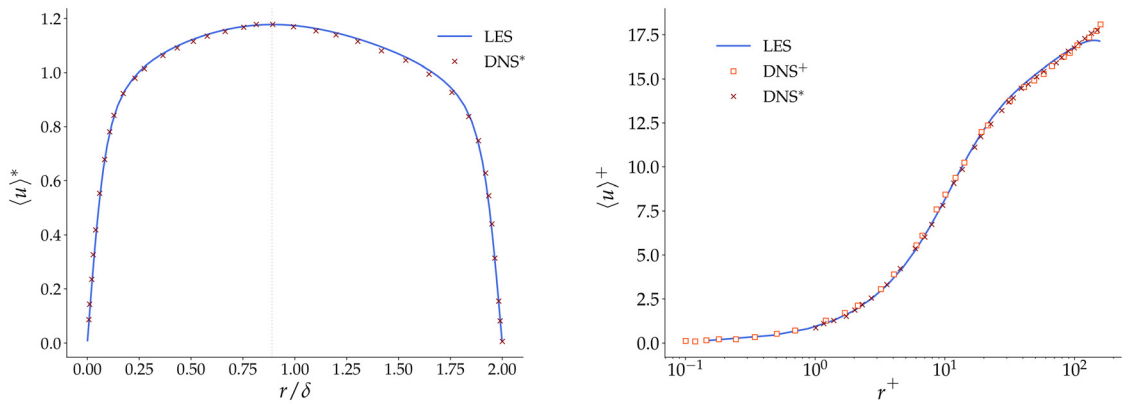

(a) (b)

FIG. 2. (a) Radial profiles of normalized averaged axial velocity on global coordinates and (b) log-law at the inner wall normalized with inner wall friction velocity. The present LES (—) is compared with DNS data from Chung *et al.*[5] (×) and Bagheri *et al.*[7] (□).

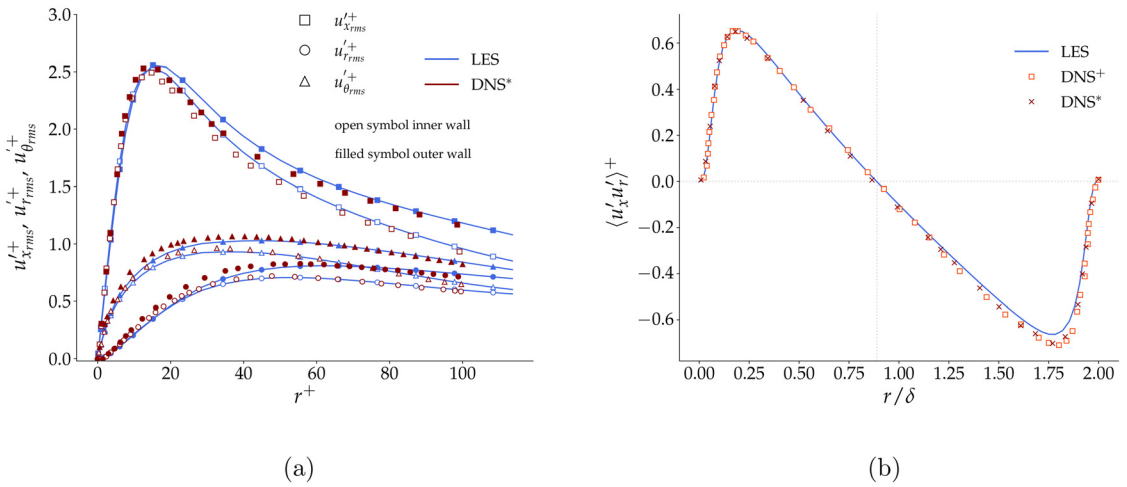

(a) (b)

FIG. 3. Reynolds stress tensor components. Root mean squared (a) and shear stress (b). Comparison with Chung *et al.*[5] (DNS*) and Bagheri *et al.*[7] (DNS+).

along the radial direction with the DNS data of Chung *et al.*[5] at $Re_{D_h} = 8900$, where the velocity normalized against the bulk velocity is indicated as $\langle u \rangle^*$. The locations $r/\delta = 0$ and $r/\delta = 2$ correspond to inner and outer walls, respectively. The distribution of the mean axial velocity is asymmetric in the radial direction, which is a distinctive feature of a concentric annular pipe flow.[1] The maximum velocity is located closer to the convex wall, at $r/\delta \simeq 0.89$, in agreement with Chung *et al.*[5] and Bagheri *et al.*[7] Overall, a quite good match is observed with the present LES results. Figure 2(b) compares the velocity profiles in the logarithmic region. The wall mean axial velocity from the LES matches the results from Chung *et al.*[5] and Bagheri *et al.*,[7] showing that the boundary layer is correctly captured in the present LES. Further validation is shown in Fig. 3(a), which compares the root mean square (r.m.s.) of velocity fluctuation components of the Reynolds stress in global coordinates. The profiles are also in good agreement with Chung *et al.*,[5] although slightly larger values are observed on the concave wall for the axial r.m.s. of velocity fluctuation component $u'^+_{x_{rms}}$, where the maximum deviation is, however, less than 3%. The Reynolds shear stress is also in very good agreement with results from Chung *et al.*[5] and Bagheri *et al.*,[7] as shown in Fig. 3(b), where the maximum deviation is on the outer wall, and less than 4% as compared to the DNS data.

In forced convection regime, the temperature behaves as a passive scalar, and its distribution is directly related to the velocity field. In Fig. 4(a), the wall modified temperature distribution is compared with the results from Marocco,[16] again showing very good agreement. Figure 4(b) provides a clear justification for the use of the term *thermal* DNS. The velocity field scales are linked to the Kolmogorov length scale, $\eta = (\nu^3/\varepsilon)^{1/4}$, with ε being the dissipation rate of turbulent kinetic energy, and the Obukhov–Corrsin length scale is the one for

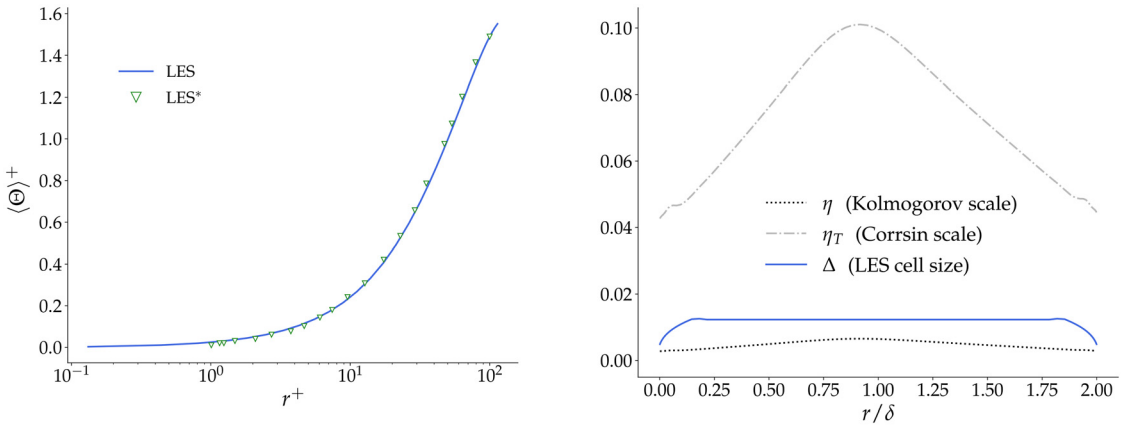

(a) (b)

FIG. 4. (a) Radial profiles of mean temperature in wall coordinates compared with the results of Marocco and Garita[18] (▽); and (b) LES mesh resolution compared with Kolmogorov and Obukhov–Corrsin scales.

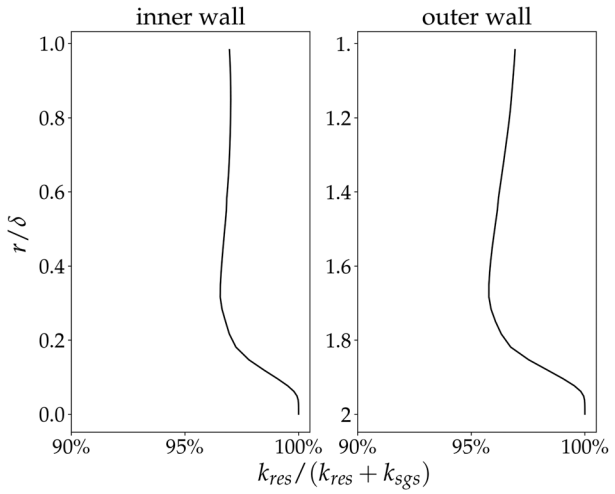

FIG. 5. Percentage ratio of the resolved (k_{res}) to total ($k_{sgs} + k_{res}$) turbulent kinetic energy along the radial direction at inner and outer walls. The quantities are averaged over time, in the streamwise and circumferential directions.

the temperature field, $\eta_T = \eta Pr^{3/4}$. As one can notice, the LES filter width $\Delta = \sqrt[3]{\mathcal{V}_{\text{cell}}}$ ($\mathcal{V}_{\text{cell}}$ is the cell volume) is significantly smaller than η_T, indicating that thermal structures are predicted with DNS resolution. The current LES methodology is thus used for the analysis in Secs. III C–III D. Under this condition, there is no need for a subgrid heat flux model. Moreover, in Fig. 5, the ratio of resolved k_{res} vs total $(k_{res} + k_{sgs})$ turbulent kinetic energy is presented, with k_{sgs} indicating the subgrid scale kinetic energy estimated as $k_{sgs} = \nu_{sgs}^2/(C_k\Delta)^2$, where $C_k = 0.094$ is a constant. As shown in the figure, the ratio is around 96% in the center of the annulus, and approaching 100% near the wall, indicating a high resolution of the turbulent scales. These resolution values correspond to a well-resolved LES.[55] Further validation of the LES methodology with magnetic field effect is presented in the Appendix.

B. Analysis of first and second order statistics with magnetic field effect

Once the LES approach is validated, it is used to investigate the interaction between the magnetic field and the fluid flow, in order to shed light on how the flow statistics are affected by their local orientation to the magnetic field. When a magnetic field is present, a relevant effect on the decay of turbulence in the conducting fluid is observed. When $Re_m < 1$, the velocity and magnetic field are uncoupled,[56] and the latter acts suppressing preferentially the Fourier components of the velocity field whose wave vector is parallel to $\mathbf{B}_0$.[20] The reason for turbulence suppression is as follows. The magnetic field is responsible for the removal of the turbulent kinetic energy, necessary to make electric currents circulate. The electric currents lead to Joule dissipation, resulting in a rise of thermal energy that corresponds to a fall in kinetic energy.[56] The energy loss follows the timescale $\tau_J = (\sigma B^2/\rho)^{-1}$, that is, the characteristic timescale of the Joule effect. This timescale is very short compared to the dissipation by viscosity that is usually related to the turn-over time of turbulent structures.[49] Another effect is that $\mathbf{B}_0$ acts anisotropically and opposes to the flow only in certain directions. The variation of turbulence structures is then dependent on the relative direction between $\mathbf{B}_0$ and the flow velocity.

The effect of the magnetic field effect is studied at three Hartmann numbers, $Ha = 40, 60, 120$. The relative strength of inertia and Lorentz force is given by Re to Ha ratio, which is Re/Ha = 222.5, 148, 74 for the three cases (Table II). According to the literature,[42,43] at these ratios, turbulence suppression and partial laminarization are expected to be observed. When Re/Ha decreases, the Lorentz force becomes more important, and the flow tends to laminarize. It is thus convenient to define three circumferential locations, depending on the relative direction of the magnetic field. Looking at Table III we identify $\theta = 0$, $\theta = \pi/4$ and $\theta = \pi/2$, where $\mathbf{B}_0$ is, respectively, perpendicular, at $\pm\pi/4$ and parallel to the walls. Figure 6(a) shows the electrical current distribution within an axial (x) section. The electric current path closes at the walls, where its intensity is maximum. The axial Lorentz force is effective at $-\pi/4 < \theta < \pi/4$, while it is almost negligible at $\theta \pm \pi/2$, as shown is Fig. 6(b), suggesting a different flow behavior depending on the relative orientation of magnetic field and flow velocity. This behavior is further emphasized in Fig. 7, which provides a 3D visualization of the velocity profile for the $Ha = 40$ case. The strong Lorentz force at $\theta = 0$ smooths out the velocity profile as observed in the figure. At $\theta = \pi/2$, the Lorentz force has instead small to no effect; thus, the velocity increases to conserve the volumetric flux. This effect on the mean velocity profile is further reported in Fig. 8(a), showing radial profiles across the three different locations defined in Table III. At $\theta = 0$, the typical Hartmann velocity profile and boundary layer are observed. Indeed, at this location, as can be noticed from Fig. 6(b), the axial Lorentz force is flipped between the near-wall region and the annulus center, resulting in an effective flattening of the velocity profile. Increasing Ha, the velocity profile becomes flatter due this effect, the boundary layer is at the same time thinner, and steep gradients are observed, as shown in Fig. 8(b), where the normalized boundary layer thickness δ_b^+ at the inner wall is plotted against the mean velocity (normalized with the asymptotic velocity u_e). Thus, the magnetic field at $\theta = 0$ breaks the typical annulus velocity asymmetry observed in Fig. 2 and forces a Hartmann velocity profile. At $\theta = \pi/2$, the velocity profile is closer to the hydrodynamic profile; however, the

TABLE II. The overview of the flow conditions simulated in the present work at $Re_D = 8900$ and $Pr = 0.026$.

Ha	0	40	60	120
Re/Ha	···	222.5	148	74

TABLE III. Circumferential positions. Symbol and line styles used.

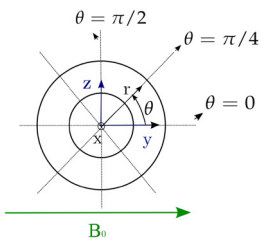

Common symbols and linestyles

△	$\theta = \pi/2$	Ha=0
□	$\theta = \pi/4$	Ha=40
○	$\theta = 0$	Ha=60
		Ha=120

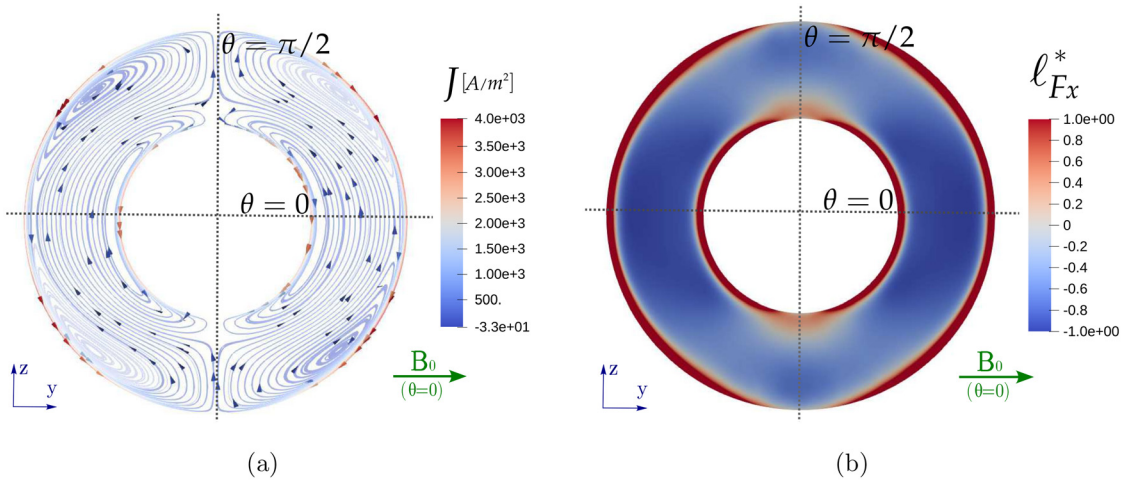

FIG. 6. Electrical currents (J) path (a) and normalized axial Lorentz force ℓ_F (b), at $Ha = 60$. Slice at $x = 12.5\delta$ (axial direction). $\mathbf{B}_0$ direction is at $\theta = 0$. Mean flow direction in positive x, exiting the page.

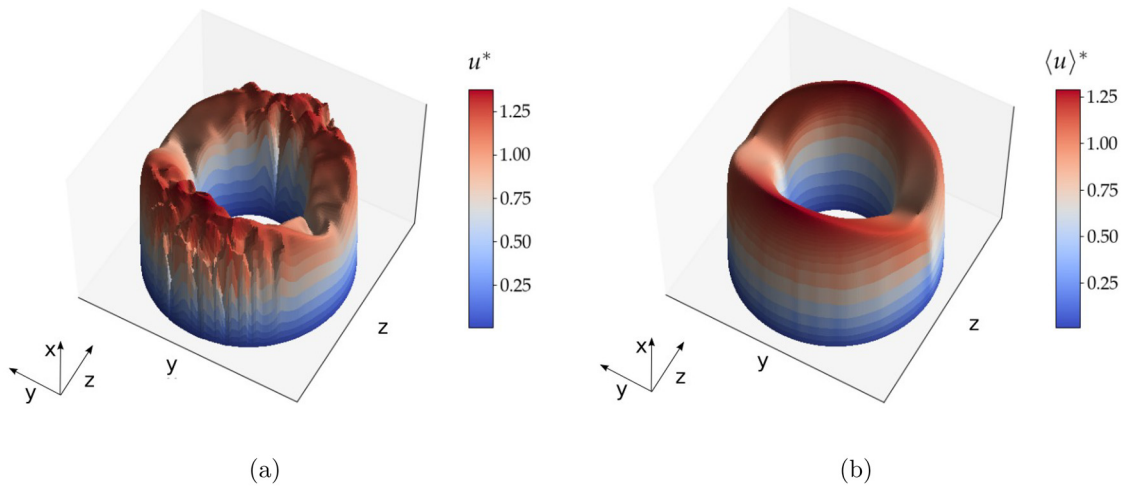

FIG. 7. 3D visualization of axial velocity profile at $Ha = 40$. Instantaneous (a) and mean (b). Mean flow direction in the positive x direction.

peak value is higher, and its location is shifted toward the center of the annulus for $Ha = 40$ and $Ha = 60$. It is interesting to notice that the mid-profile ($\theta = \pi/4$) shows a completely different behavior: the maximum velocity is now located closer to the outer wall. This effect is enhanced when increasing the Hartmann number, and it is due to the larger axial Lorentz force on the outer wall at this location. This velocity profile is peculiar to this geometry, and it has not been observed in other studies. Moreover, the observations indicate that at this location, the Lorentz force still prevails on inertia and that the magnetic effect on the outer wall is stronger than on the inner wall. Detailed views of these effects are clearly visible in the two zoom-in zones of Fig. 8(a), respectively, at inner [Fig. 8(c)] and outer [Fig. 8(d)] walls. More details on the velocity profile modification are added by Figs. 9(a) and 9(b) that show the near wall velocity at the inner and outer walls. At $\theta = \pi/2$, the profiles follow the hydrodynamic shape until $r^+ \approx 10$. However, the major difference is observed at $\theta = \pi/2$ for $Ha = 120$, where the slope grows after $r^+ \approx 13$ and no clear logarithmic shape is present before $r^+ \approx 100$. At $\theta = 0$, and $Ha = 120$, the logarithmic range becomes shorter, and the viscous sub-layer tends to differ from $u^+ \sim r^+$ after $r^+ \approx 2$. A further observation is the plateau in Fig. 9(a) at $\theta = 0$ for $Ha = 60$ (from $r^+ \approx 50$) and $Ha = 120$ (from $r^+ \approx 30$), whose width increases with Ha, similarly to the results obtained by Boek *et al.*[32] for a channel flow. Moreover, there is no difference, at this location, between outer and inner walls, confirming the velocity symmetry observed in Fig. 8(a). These observations suggest the presence of quasi 2D turbulence. In fact, the plateau observed at $\theta = 0$ is a feature in line with the idea of quasi 2D turbulence, as suggested by Knaepen and Moreau.[41]

So far, the alteration of the velocity profile, due to the magnetic field, has been presented; however, as mentioned in Sec. I, one of the

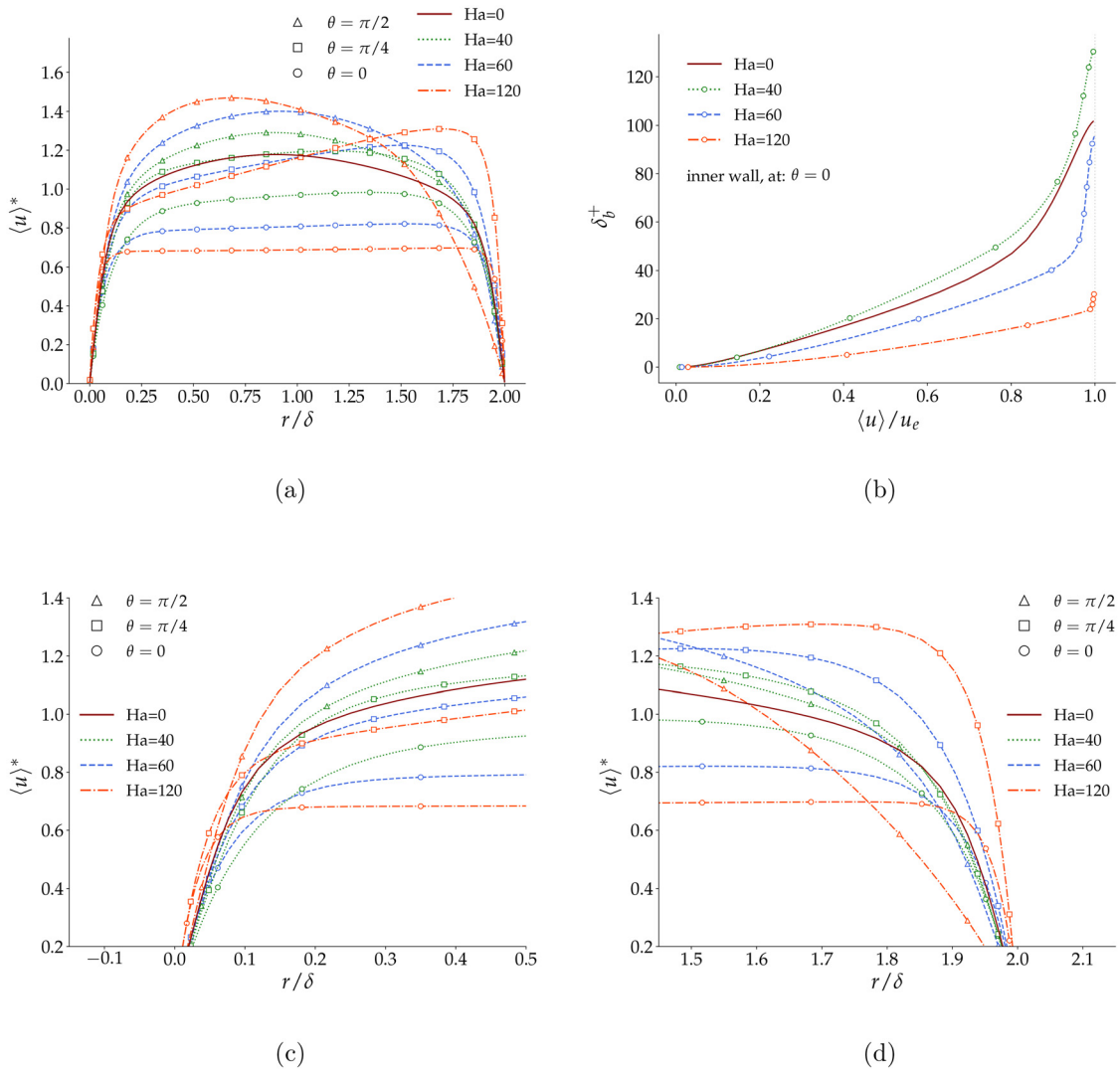

FIG. 8. Mean axial velocity profile (a), normalized displacement boundary layer thickness (b), and zoom-in view of the mean axial velocity at inner (c) and outer (d) walls. The $()^*$ symbol defines normalization against the bulk velocity, while u_e represents the asymptotic velocity.

main outcomes of the magnetic conditioning is related to the turbulence modification. An initial overview of this effect can be obtained analyzing the Reynolds stress tensor components. In Fig. 10, the Reynolds shear stress is presented. At $\theta = 0$, the Reynolds shear stress is negligible compared to the $Ha = 0$ case, indicating very large turbulence suppression for the directions whose wall is perpendicular to the magnetic field, in agreement with the literature. At $\theta = \pi/4$ and $Ha = 120$, the profile shows an inversion of trend, in agreement with the inversion of trend observed for the mean velocity in Fig. 8(a). The latter is peculiar of the concentric annulus, and it is not observed in previous studies. At $\theta = \pi/2$, the turbulent shear stress resembles the hydrodynamic profile for the $Ha = 40$ and the $Ha = 60$ cases, although smaller peaks are observed, which is a sign of less effective turbulence suppression in this direction. The Reynolds shear stress component analysis, thus, indicates strong turbulence suppression at $-\pi/4 < \theta < \pi/4$ for $Ha = 40$ and $Ha = 60$. At $Ha = 120$, the suppression is observable at all circumferential positions, denoting that the Lorentz force largely prevails on inertia at this Re/Ha ratio. For the $Ha = 120$ case, the turbulence contribution to the total shear stress is, in fact, negligible, implying that the total shear stress tends to be mostly viscous at low Re/Ha ratio. Moreover, the level of Reynolds shear stress suppression differs from what observed in a square duct, where larger turbulence dumping is observed at higher Re/Ha. In Blishchik and Kenjereš,[57] at $Re/Ha = 265$, $\langle u_x' u_r' \rangle$ at the sidewall of their squared duct was observed to drop of about 35%, while in the annulus at $Re/Ha = 222.5$, only of 15%, i.e., the annulus flow is more *turbulent* at this Re/Ha.

The previous analysis provided a glimpse of the turbulence suppression. However, a more thorough study requires the investigation of the main components of the Reynolds stress tensor. In Fig. 11,

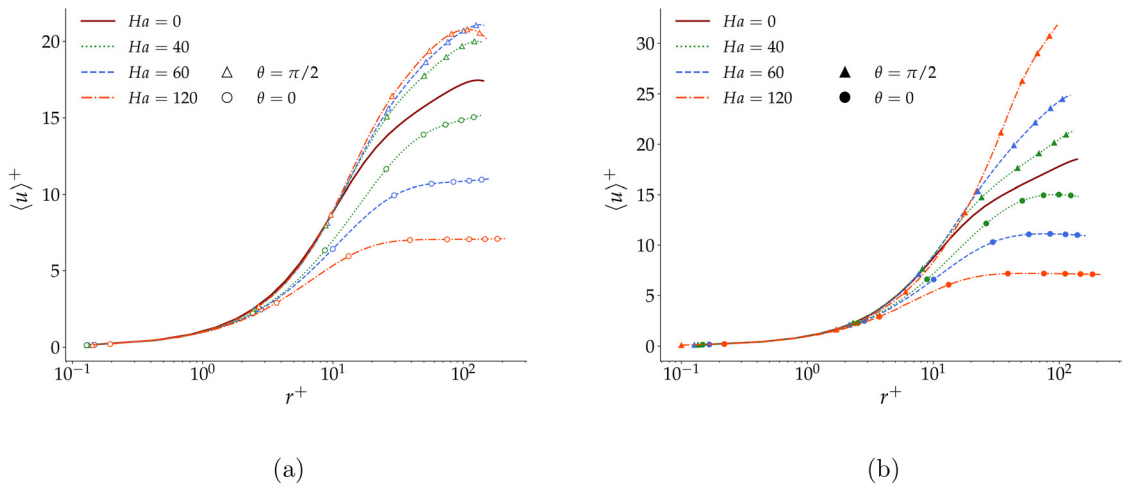

FIG. 9. Near-wall mean velocity at inner (a) and outer (b) walls in wall coordinates. Comparison at $Ha = 0, 40, 60, 120$.

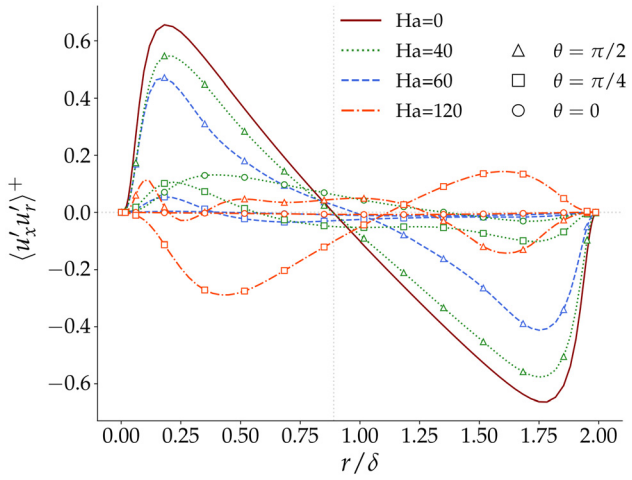

FIG. 10. Reynolds shear stress in global coordinates. The profiles at $\theta = 0$ (°) are mostly negligible.

the r.m.s. of velocity fluctuation components are shown. The axial component $u_{x_{rms}}{}'$ at $\theta = \pi/2$ in Figs. 11(a) and 11(b) for the $Ha = 40$ and the $Ha = 60$ cases is very similar to the $Ha = 0$ case, indicating that the magnetic field has a limited effect at this location. However, at $Ha = 120$, $u_{x_{rms}}{}'$ has a different shape and its peak is located at $r^+ \approx 80$ on the outer wall [Fig. 11(b)], in contrast with the shape observed for the inner wall. The axial fluctuation is instead significantly reduced at $\theta = 0$, and it approaches a plateau at $r^+ \sim 30$ and $r^+ \sim 10$, respectively, for $Ha = 60$ and $Ha = 120$. Very different shapes are observed between inner and outer wall for the $Ha = 40$ case at $\theta = 0$ as shown in Figs. 11(a) and 11(b). The analysis of the radial r.m.s. of velocity fluctuation component $u_{r_{rms}}{}'$, in Figs. 11(c) and 11(d), indicates a consistent suppression of this component as the Hartmann number increases. Eventually, at $\theta = 0$, this component approaches zero for $Ha = 60$ and $Ha = 120$, indicating a preferential suppression of components parallel to the magnetic field lines, in agreement with the results for the Reynolds shear stress in Fig. 3(b). Different suppression levels are observed between the inner and outer walls for the $Ha = 40$ case, denoting stronger suppression on the outer wall. The azimuthal component, $u_{\theta_{rms}}{}'$ instead, in Figs. 11(e) and 11(f), shows a completely different behavior. At $Ha = 40$, its amplitude decreases both at inner and outer walls. Unlike the other components, for a further increment of Ha, the azimuthal component amplitude increases. This feature can be observed at both inner and outer walls, and at both $\theta = 0$ and $\theta = \pi/2$. At $Ha = 120$, the azimuthal r.m.s. of velocity fluctuation component is even larger than the case without magnetic field. This implies a different flow behavior for this geometry, depending on the Re/Ha ratio that is characterized by suppression of some velocity fluctuations (radial and streamwise) and enhancement of others (azimuthal). Moreover, it is interesting to notice from Figs. 11(e) and 11(f), that for both $Ha = 60$, $Ha = 120$, the azimuthal component amplitude has the same magnitude as the respective axial component, which is also a feature not observed in previous studies. The decay of the velocity component parallel to the magnetic field is instead in line with previous studies,[29,38] as well as the suppression of the transversal component, except for the azimuthal component. The reason for this has to be linked to the different walls curvature and to the genesis of a new flow regime defined by the Re/Ha ratio, in which turbulence can appear in a non-conventional state.

As mentioned at the beginning of this section, the magnetic field extracts turbulent kinetic energy to feed the electric currents. In Figs. 12(a) (convex wall) and 12(b) (concave), this aspect is illustrated. The profiles of turbulent kinetic energy k shown in the figures are consistent with the r.m.s. of velocity fluctuations components in Fig. 11, and large values of turbulent kinetic energy are observed at $\theta = \pi/2$ for all Hartmann numbers, confirming that at this location the flow is still turbulent. On the concave wall, in Fig. 12(b), the peak value for the $Ha = 120$ case is in agreement with the values of $u'_{\theta_{rms}}$ and $u'_{x_{rms}}$ observed in Figs. 11(b) and 11(f). At $\theta = 0$ and $\theta = \pi/4$, the kinetic

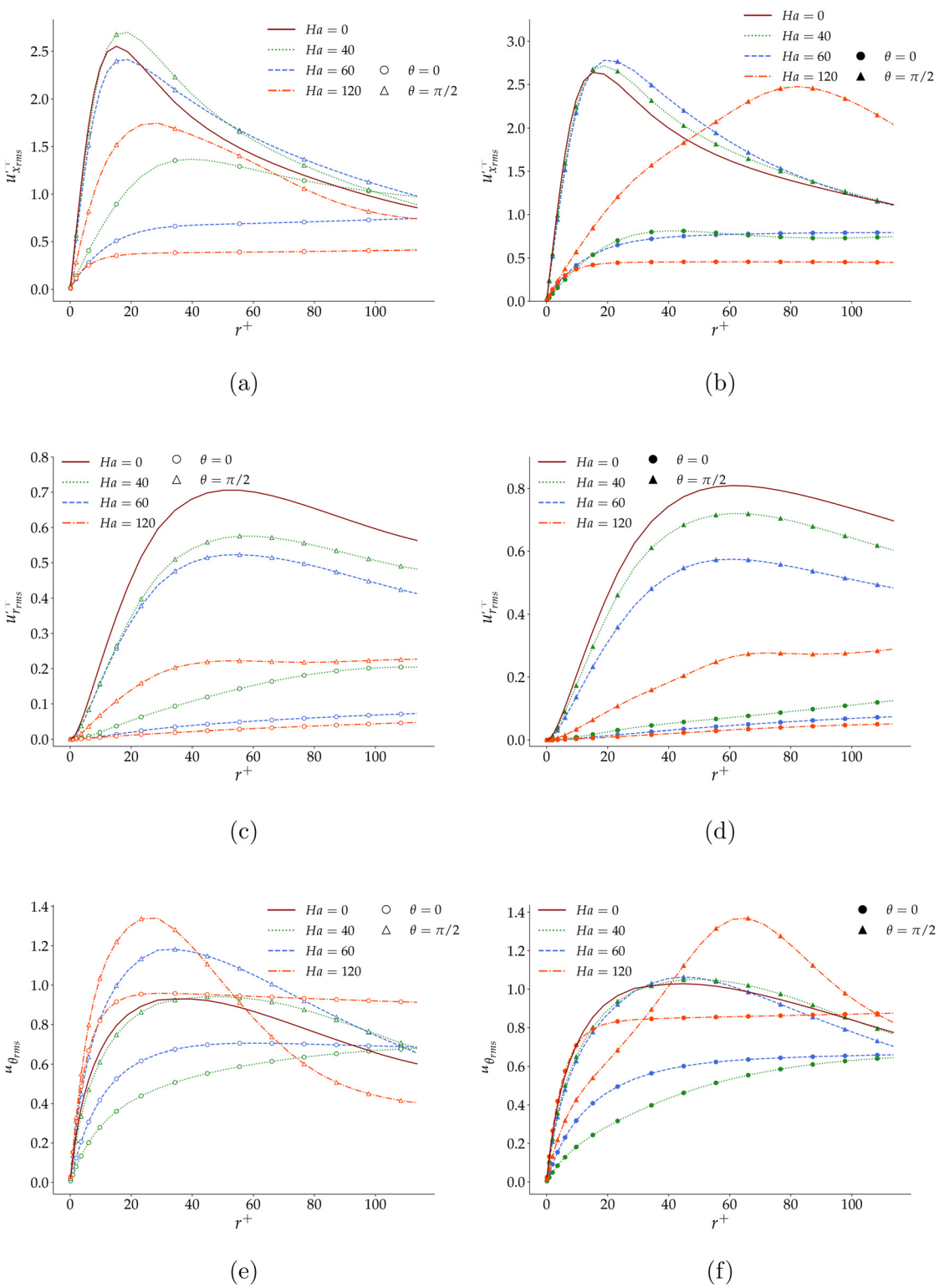

FIG. 11. r.m.s. of velocity fluctuation components at the inner [(a), (c), and (e)] and outer [(b), (d), and (f)] walls, normalized by the respective mean friction velocity, for different *Ha* and two different azimuthal locations.

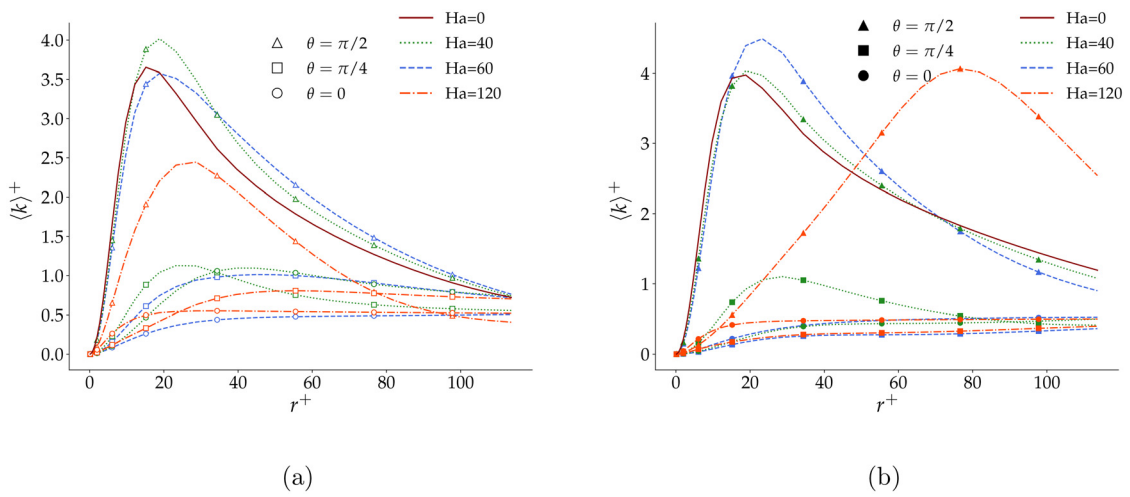

FIG. 12. Local turbulent kinetic energy at inner (a) and outer (b) walls, for different *Ha* and azimuthal locations.

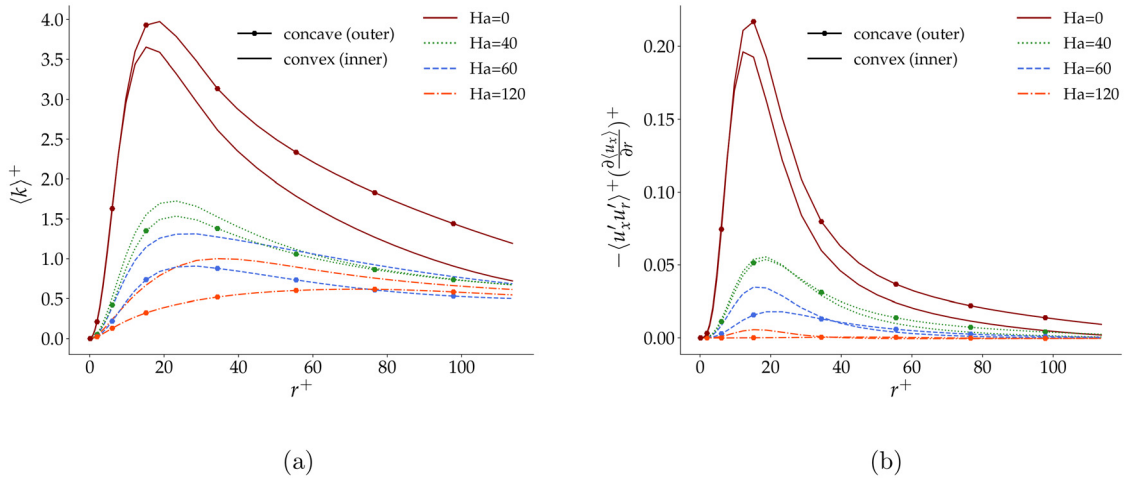

FIG. 13. Mean turbulent kinetic energy (a) and mean turbulent kinetic energy production (b) at inner and outer walls for different Hartmann numbers.

energy is significantly reduced for all Hartmann numbers. Overall, the turbulent kinetic energy is consistently reduced by an increase in Hartmann number, as shown in Fig. 13(a), where the circumferential average turbulent kinetic energy is shown. Moreover, one can notice that the turbulent kinetic energy is larger on the convex wall for all cases with $Ha \neq 0$, in contrast with the non-magnetic case. This effect is related to the electric currents (i.e., the Joule effect) observed on the outer wall, indicating that $\mathbf{B}_0$ extracts more kinetic energy from the flow on the outer wall than on the inner wall. Similar observations can be made by looking at Fig. 13(b), which shows the normalized turbulent kinetic energy production, defined as

$$\mathcal{P} = -\langle u_r' u_x' \rangle^+ \left(\frac{\partial \langle u_x \rangle}{\partial r} \right)^+. \tag{15}$$

The peaks in this case are located closer to the walls as compared to the kinetic energy case. It is clear from the figure that at the inner wall, more energy is produced, in respect to the outer wall, when a magnetic field is present. The production consistently drops when increasing the Hartmann number; indeed, it is very close to zero for $Ha = 120$, suggesting that a further decrease in the *Re*/*Ha* ratio would eventually lead to total turbulence suppression and complete flow laminarization.

The previous results show the effects of the magnetic field on the flow field. These effects also affect the wall friction, which indeed varies around the circumferential direction. Table IV reports the circumferentially averaged skin friction coefficient, $C_f = \tau_w/(0.5\,\rho\,U_b^2)$, normalized by its value at $Ha = 0$, and Fig. 14 shows its variation from $\theta = 0$ to $\theta = \pi/2$. Contrary to the $Ha = 0$ case, where C_f is larger on the inner wall,[5,16] the skin friction is larger on the outer wall and increases with the Hartmann number. At $Ha = 40$, the skin friction coefficient is smaller than the $Ha = 0$ case (on the inner wall). This effect is apparently due to the drag reduction, indicating that at this *Re*/*Ha* ratio, the turbulence suppression effect is larger than the drag increase due to

TABLE IV. Averaged skin friction value at different Hartmann numbers.

	$Ha = 40$	$Ha = 60$	$Ha = 120$
$(C_f/C_{f_{Ha=0}})_i$	0.95	1.1	1.75
$(C_f/C_{f_{Ha=0}})_o$	1.01	1.25	2.18

Hartmann effect. At $Ha = 60$ and $Ha = 120$, and at $\theta = 0$, the convex and concave wall skin frictions are about the same for the same Ha, in agreement with the fact that in this position the velocity profile is symmetric. The maximum skin friction is observed on the outer wall at $\theta = \pi/4$, as opposed to the results of Satake *et al.*[24] that observed the maximum at $\theta = 0$ for a pipe flow. This outcome is related to the velocity profile observed in Fig. 8(a) at $\theta = \pi/4$, that shows a thin boundary layer close to the outer wall. Overall, the skin friction tends to increase, decreasing the Re/Ha ratio. This increment is not due to turbulence (that in fact decreases), but to the modification of the velocity profile via the formation of thin boundary layers (Hartmann boundary layers).

In general, the results above show that the main magnetic field effects are related to the decay of turbulent kinetic energy and to the preferential suppression of turbulence, in agreement with the available literature. However, due to the different wall curvatures, the mean quantities are reorganized depending on their circumferential location, and their qualitative behavior are inherently different from the ones that can be observed in a pipe flow. Moreover, at low Re/Ha ratios, the azimuthal velocity fluctuation amplitude becomes comparable to the streamwise velocity fluctuation. This suggests the presence of non-conventional turbulence, owing to the formation of two-dimensional turbulent states, which will be further discussed in Sec. III D.

C. Temperature field

In this section, the aim is to analyze the magnetic field effect on temperature distribution for the case of forced convection, in order to understand how the modified flow statistics affect the annulus heat transfer characteristics. The modified temperature distribution is presented in Fig. 15, in global coordinates, where Θ_b is normalized by the

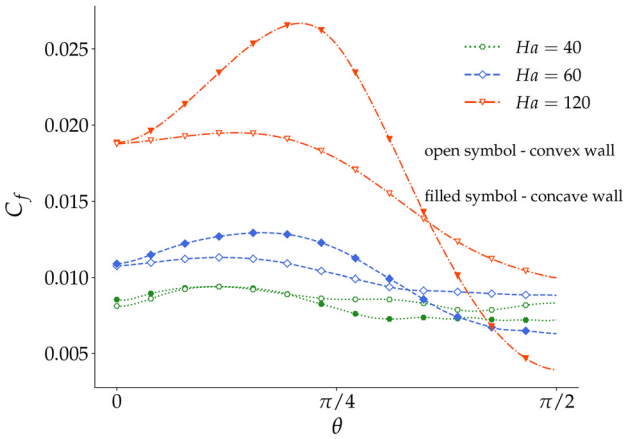

FIG. 14. Friction coefficient on inner and outer walls from $\theta = 0$ to $\theta = \pi/2$.

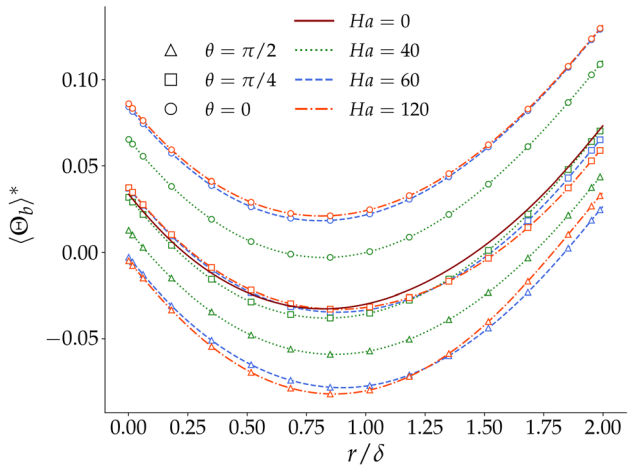

FIG. 15. Temperature distribution in global coordinates. Normalized by the reference temperature T_{ref}.

reference temperature $T_{ref} = qD_h/(\alpha\rho c_p)$. Higher temperatures are predicted at the outer wall due to its larger surface. The temperature profiles have similar shape for each of the cases studied, and only shift vertically on the vertical axis, depending on circumferential location and Hartmann number, because of the different velocity profile observed in Fig. 8(a). For all Ha, the profiles resemble those of a laminar flow, indicating that turbulence suppression does not significantly affect the mean temperature distribution. This is further observed in Figs. 16(a) and 16(b), where the axial and radial turbulent heat flux are plotted in global coordinates. The axial heat flux $\langle u_x'\Theta_b'\rangle^+$ for $Ha = 40$ at $\theta = \pi/2$ tends to maintain the shape observed for $Ha = 0$ and the local minima and maxima are very close, indicating a negligible magnetic field effect at this location. At $Ha = 60$, larger values are encountered for both $\theta = 0$ and $\theta = \pi/2$, mainly due to larger temperature fluctuations (not shown). The radial position where $\langle u_r'\Theta'\rangle^+$ equals zero divides the inner and outer thermal boundary layers. At this position, in agreement with the velocity profile, the mean temperature Θ_m also reaches its minimum as shown in Fig. 15 for $Ha = 0$. At $\theta = 0$, the radial heat flux is negligible for the three Hartmann numbers, since the velocity radial component is the most affected by magnetic field suppression, as observed in Figs. 11(c) and 11(d). At $\theta = \pi/2$ and for $Ha = 40$, the radial turbulent heat flux is asymmetric like the $Ha = 0$ case, but its magnitude is slightly reduced, and the point of zero radial turbulent heat is more toward the center of the annulus. Similar profiles are observed at $Ha = 60$ and $Ha = 120$. It is worth noting, by looking at Fig. 17, that the radial turbulent heat transfer has small to no effect on the total heat transfer. The total heat flux is given by the sum of the radial turbulent heat and the molecular heat flux. The latter is given by the following equation:

$$\chi = \frac{1}{Pr}\left(\frac{\langle d\Theta_b\rangle}{dr}\right)^+. \tag{16}$$

Figure 17 compares, thus, the heat fluxes at $Ha = 0$ and $Ha = 120$. The molecular heat flux is very similar at every θ. For both Ha cases, the contribution of the turbulent heat transfer is small compared to the molecular one, because of the large thermal conductivity of liquid

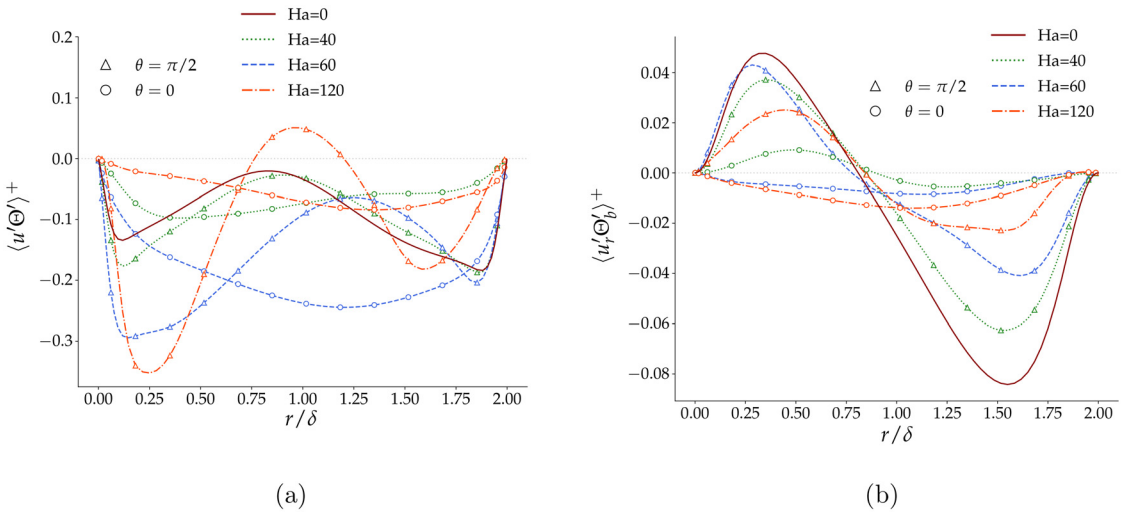

FIG. 16. Axial (a) and radial (b) heat fluxes distribution in global coordinates. Normalized by the reference temperature T_{ref}.

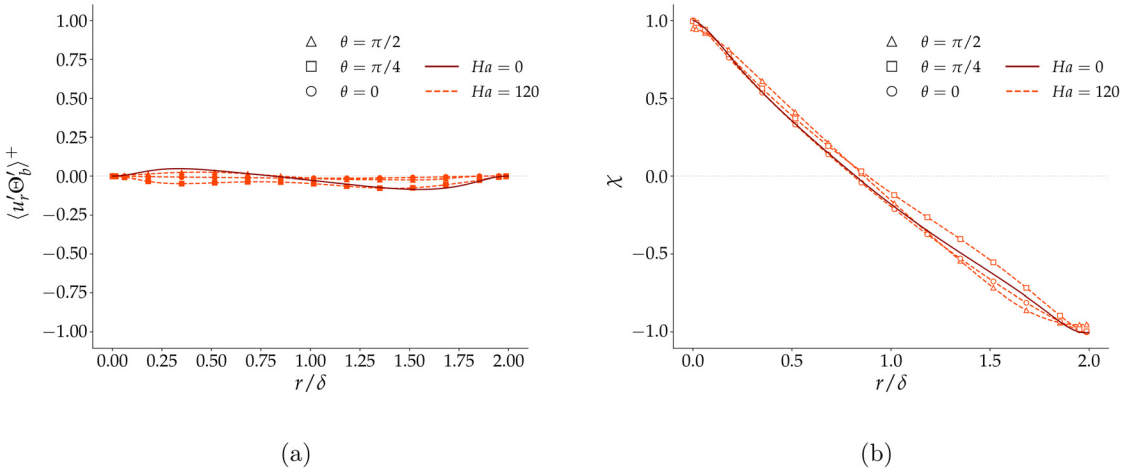

FIG. 17. Turbulent (a) and molecular (b) heat transfer in global coordinates, normalized by the friction velocity and temperature at $Ha = 0$ and $Ha = 120$.

metals, which makes heat transfer very conductive at relatively low Reynolds numbers. For this reason, the turbulence suppression does not affect much the heat transfer characteristics in forced convection.

Overall, the analysis above shows that the magnetic field affects the temperature characteristics throughout the modification of the velocity profile only, while turbulence suppression has no direct effect since heat transfer is mostly conductive in liquid metals.

D. Coherent structures and anisotropy

The effect of the magnetic field has been analyzed in Secs. III B–III C through first and second order flow statistics. The aim of this section is to examine more in detail the modification of turbulence structures. This is achieved by visualizing the streaks in the near-wall region, analyzing the correlation functions and the fluid flow anisotropy.

It is well-known that there are two key structures in the near-wall region: streamwise vortices and streaks. Streaks are zones of slowly moving fluid stretched in the direction of the mean flow, and they are observed in all developed near-wall turbulent flows. Numerical simulations show that if streaks are suppressed, the turbulence intensity is substantially reduced.[58] Streamwise vortices produce streaks through the deformation of the mean flow by their induced cross-flow advection. The streaks, which tend to be uniform in the streamwise direction, become unstable, bending along the streamwise direction and inducing the production of streamwise vorticity. In this manner, streaks and streamwise vortices consequently form each other in order to maintain near-wall turbulence.[59] Figure 18 shows the near-wall streaks, visualized using axial velocity fluctuations u'_x, normalized by the friction velocity u_τ. When no magnetic field is present, regular pattern structures alternate in the axial and azimuthal directions as shown

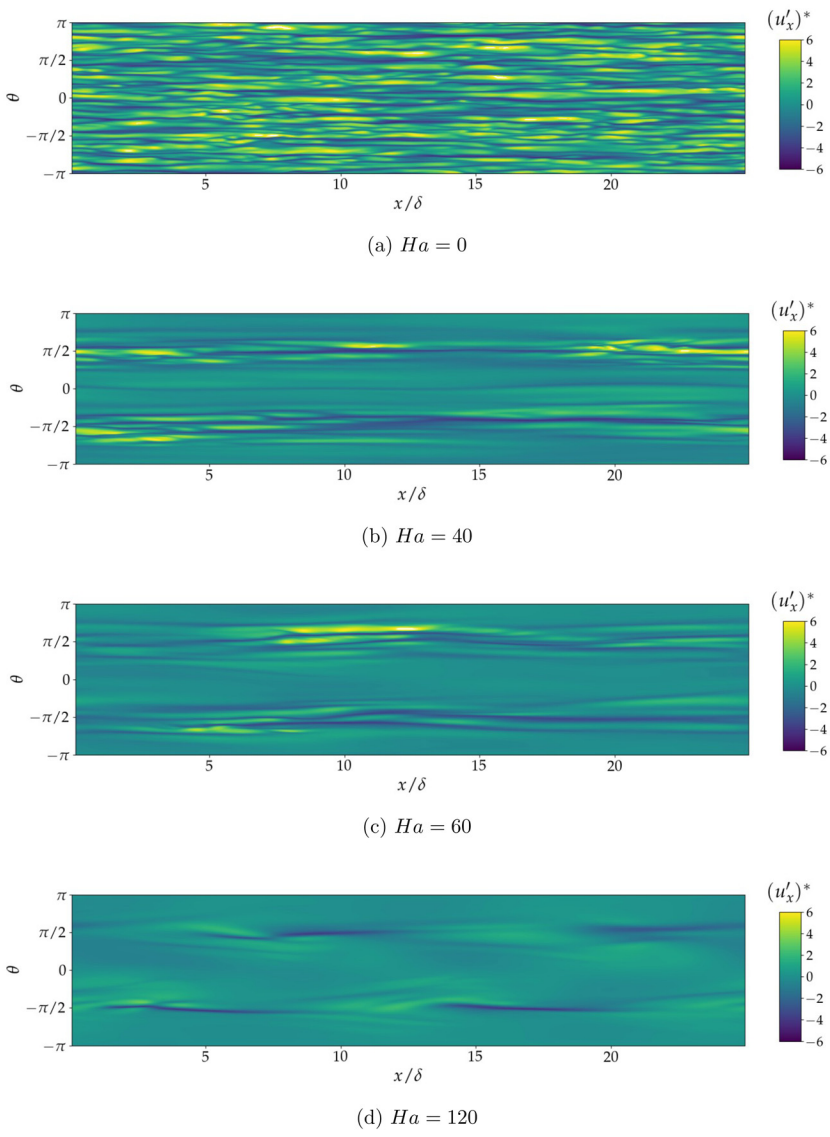

FIG. 18. Axial velocity fluctuation contour at $r^+ \approx 10$ from the inner wall, normalized with the respective mean friction velocity. Cases $Ha = 0$ (a), $Ha = 40$ (b), $Ha = 60$ (c), and $Ha = 120$ (d).

in Fig. 18(a), where the highly elongated zones of high-speed ($u'_x > 0$) and low speed flow ($u'_x < 0$) alternated. When the magnetic field is applied, no streaks are observed at $\theta = 0$ and $\theta = \pi$ at any Hartmann number. Moreover, the streaks are elongated in the streamwise direction and reduced in magnitude, as shown in Figs. 18(b)–18(d). Similar observations can be made for the azimuthal component u'_θ in Fig. 19. It is clear that the magnetic field tends to suppress near wall streaks at $\theta = 0$ (Hartmann wall), while their elongation in the streamwise direction is observed at $\theta = \pi/2$ (sidewall).

In order to investigate these turbulent structures quantitatively, an analysis of correlations is also presented here. The correlation function contains information about vortical structures present in turbulent flows and provides an overview of the scales of coherent structures. Since the integral scales are related to the correlation functions, this analysis also provides an indication of the largest eddies dimension. The two-point correlation function is used for this purpose, which on the x direction can be expressed as follows:

$$R_{uu}(a) = \frac{\langle u'(\mathbf{x}, t)u'(\mathbf{x} + a, t)\rangle}{\langle u'(\mathbf{x}, t)u'(\mathbf{x}, t)\rangle}, \tag{17}$$

a being the axial separation distance. The correlations are computed at $\theta = \pi/2$, along the x direction, and at a distance from the inner wall of $r^+ \approx 35$. Figure 20 shows that $R_{uu}(a)$ approaches zero for $x/\delta > 5$ for each Ha case, suggesting that the domain chosen is appropriate. The oscillation behavior in the $Ha = 120$ case indicates a physically correlated behavior for this component. The computation has also been performed at $r^+ \approx 6$, $r^+ \approx 14$ and $r^+ \approx 21$ (not shown here) showing similar results.

An alternative to analyze the characteristic coherent structure is to work with wave numbers rather than eddy size. Using the Fourier

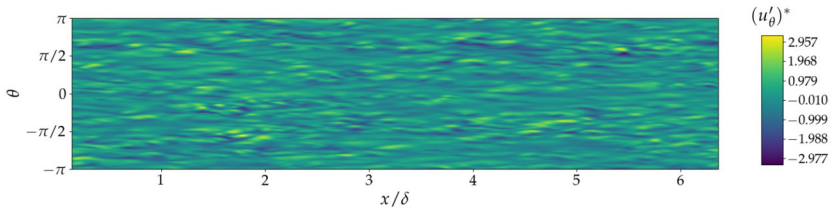

(a) $Ha = 0$

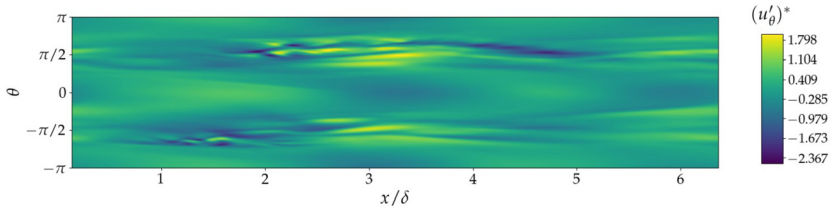

(b) $Ha = 60$

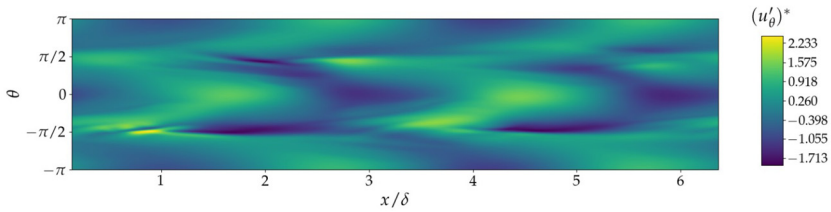

(c) $Ha = 120$

FIG. 19. Azimuthal velocity fluctuation contour at $r^+ \approx 10$. Cases $Ha = 0$, $Ha = 60$, and $Ha = 120$.

transform, one can obtain the energy spectrum, introduced via the transform pair

$$E_{ij}(\kappa) = \frac{1}{\pi}\int_{-\infty}^{\infty} R_{ij}(s)e^{-iks}ds \tag{18}$$

with s being the spatial coordinate and k the wave number. $E_{ij}(\kappa)$ is a measure of how energy is distributed across various eddy sizes, and it is referred to as the 1D energy spectrum. $\kappa = n\kappa_0$ is the wave number, where κ_0 is the lowest positive wave number, defined as $\kappa = 2\pi/L_x$, with the integer $n \in [-N/2, N/2]$ for N sample points. In Fig. 21(a), the 1D energy spectrum of the axial component is shown. Most of the energy is contained at the lowest wave numbers (large eddies), and the energy content at certain scale seems to decrease for the axial and radial directions as Ha increases [Figs. 21(a) and 21(b)]. The energy content in the azimuthal direction is observed instead to increase with the Ha at large scales and decrease only for high wave numbers. This observation suggests a reorganization of turbulence structures, leading to a re-energization of the velocity azimuthal component. In fact, one of the effects of the magnetic field, as mentioned in Sec. III B, is the anisotropic influence of the magnetic field on turbulence. Following the idea of Lumley,[60] the stress tensor can be divided in the traceless deviatoric part a_{ij} and an isotropic part. The normalized anisotropy tensor is defined as

$$b_{ij} = \frac{a_{ij}}{2k} = \frac{\langle u_i u_j \rangle}{2k} - \frac{1}{3}\delta_{ij} \tag{19}$$

with k being the kinetic energy. The principal components of the anisotropic tensor are then obtained as

$$I_1 = tr(\mathbf{H}), \tag{20}$$

$$I_2 = \frac{1}{2}(tr(\mathbf{H})^2 - tr(\mathbf{H}^2)), \tag{21}$$

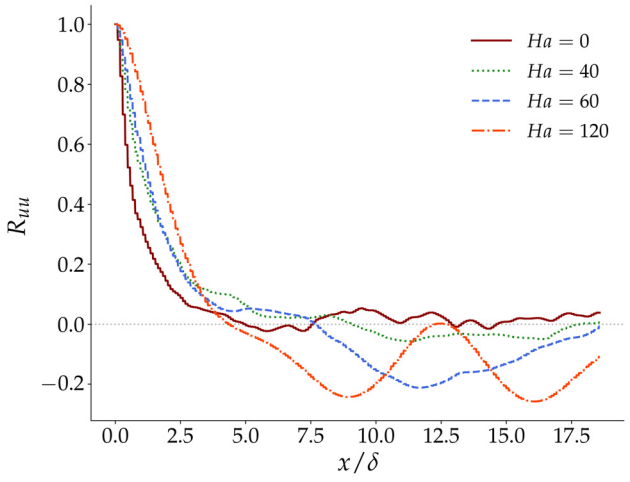

FIG. 20. Velocity correlations in the axial direction at distance from inner wall of $r^+ \approx 35$ and at $\theta = \pi/2$ (sidewall location).

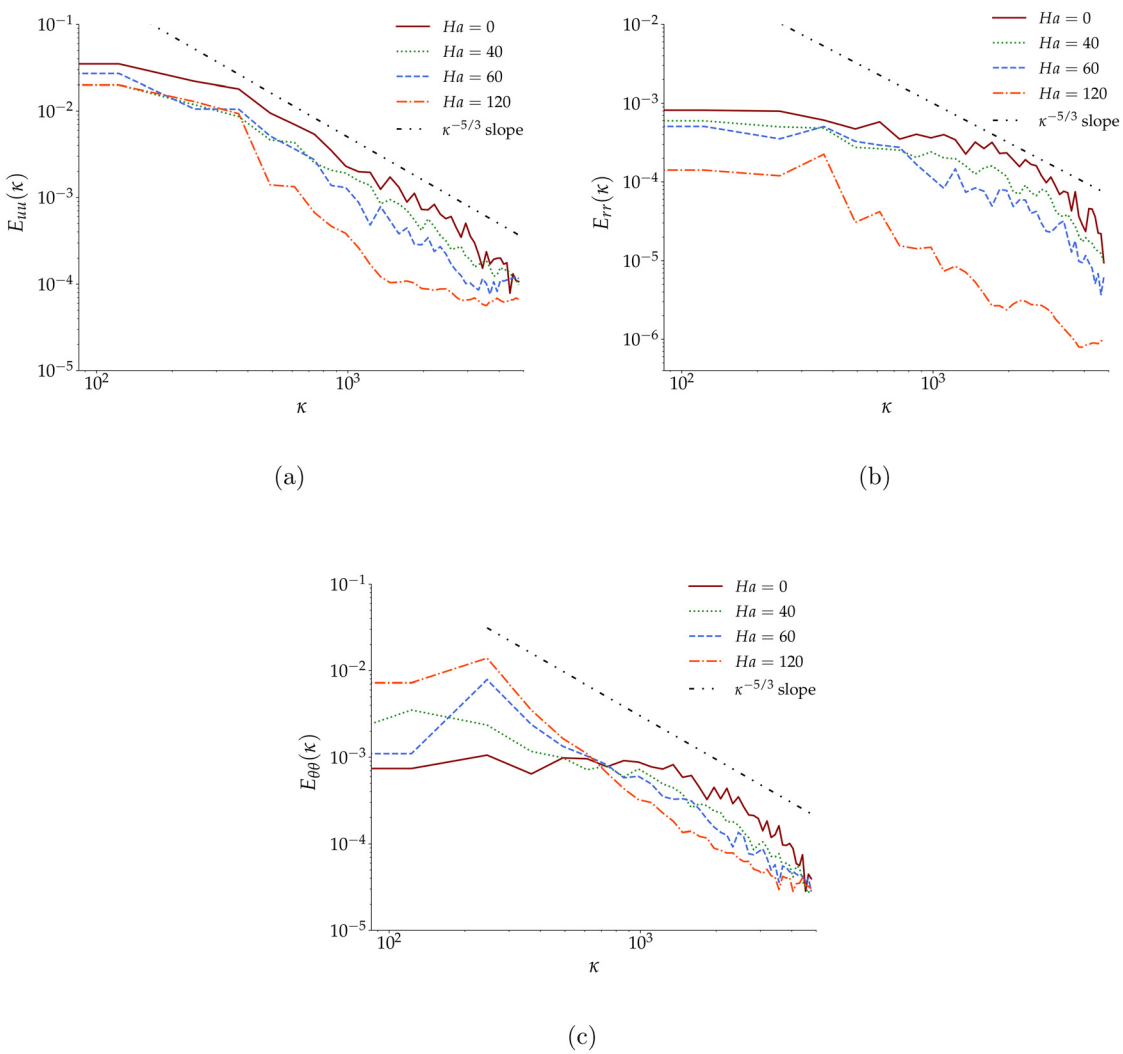

FIG. 21. 1D Energy spectrum. Axial (a), radial (b), and azimuthal (c) components. Cases $Ha = 0$, 40, 60, 120. Data collected at $\theta = \pi/2$, at $r^+ \approx 35$.

$$I_3 = det(\mathbf{H}), \tag{22}$$

where *tr* and *det* refer, respectively, to the trace operator and the determinant. I_k refers to the first, second, and third invariants of the normalized anisotropy tensor $\mathbf{H}$ (with b_{ij} as components). I_1 is always zero for incompressible flows, and the $I_2 = I_3 = 0$ condition represents an isotropic state. Intermediate states are summarized in Table V. For a pipe flow, one can expect to observe two-component close to the wall and an isotropic state along the centerline.[62] In Figs. 22(a)–22(c), an anisotropic map is plotted for a line going from the inner wall to the centerline. For the $Ha = 0$ case, near the wall, turbulence appears in a two-component state, heading toward the one component state, as one moves away from the wall up to $r^+ \approx 7$. After this position, the turbulence starts following the $I_3 > 0$ curve, indicating an axisymmetric expansion. In this position, turbulence has a rod-like shape, due to a principal larger component and the other two component of similar intensity. Moving toward the centerline, the isotropic state is approached. A similar behavior is observed for $Ha = 40$ at $\theta = \pi/2$. At $\theta = 0$, instead, starting from a two-component behavior near the wall, the turbulence never follows the positive axisymmetric line (I_3) and stays very close to the two-component line, thus maintaining a disk-like shape. Even on the centerline, no isotropic turbulence is observed. For the $Ha = 60$ case, the previous effect is more evident at $\theta = 0$, and independently of the radial position, turbulence appears on the two-component limit, indicating the presence of only two components of similar intensity. The $\theta = \pi/2$ profile is also deviating from the case with no magnetic field, as shown in Fig. 22(b). At $Ha = 120$, Fig. 22(c), a further change in turbulence state is observed. At $\theta = 0$, the entire profile is in the two-component axisymmetric state. The difference between the $Ha = 60$ and $Ha = 120$ cases is likely due to the growth of the azimuthal component observed in Fig. 3(a). Indeed, by looking again at Figs. 11(a) and 11(e), one can notice that the values of $u'_{x_{rms}}$ and $u'_{\theta_{rms}}$ are comparable for the $Ha = 60$ case, while larger differences are observed for the $Ha = 120$ case. At $\theta = \pi/2$, the turbulence state no longer resembles the $Ha = 0$ case, and the profile is

TABLE V. Description of turbulent anisotropy states over Lumley triangle.[61] Each state is linked to the respective shape and value of the invariants.

Shape	Turbulent state	Invariants
	Isotropic	$I_3 = I_2 = 0$
	Two component axisymmetric	$I_3 = -\frac{1}{108}, \quad I_2 = -\frac{1}{12}$
	Two component	$I_3 = -(I_2/3 + 1/27)$
	One component	$I_3 = \frac{2}{27}, \quad I_2 = -\frac{1}{3}$
	Axisymmetric ($I_3 > 0$)	$I_3 = 2(-I_2/3)^{3/2}$
	Axisymmetric ($I_3 < 0$)	$I_3 = -2(-I_2/3)^{3/2}$

contained between the two-component and the positive axisymmetric line. Next, it is interesting to look at how the near-wall turbulence is modified along the circumferential direction. Figure 22(d) presents the Lumley triangle for a line along the azimuthal direction from $\theta = 0$ to $\theta = \pi/2$, at a distance from the wall of $r^+ \approx 5$. When no magnetic field is present, only the two-component axisymmetric state is observed. A similar state is observed for the $Ha = 40$ case. At $Ha = 60$, at $\theta = 0$, the two-component axisymmetric state is observed and, moving along the circumferential direction, the profile moves on the two-component line. At $Ha = 120$, turbulence is on the two-component line at $\theta = 0$, and moving along the circumferential direction, it approaches first the two-limit component at $\theta = \pi/4$, then moves toward the positive axisymmetric limit to finally re-approach the two-component state at $\theta = \pi/2$.

The anisotropy map indicates how turbulence changes, in response to the magnetic field. In particular, the analysis above shows 2D and 3D turbulent states coexist at different ranges of Re/Ha,

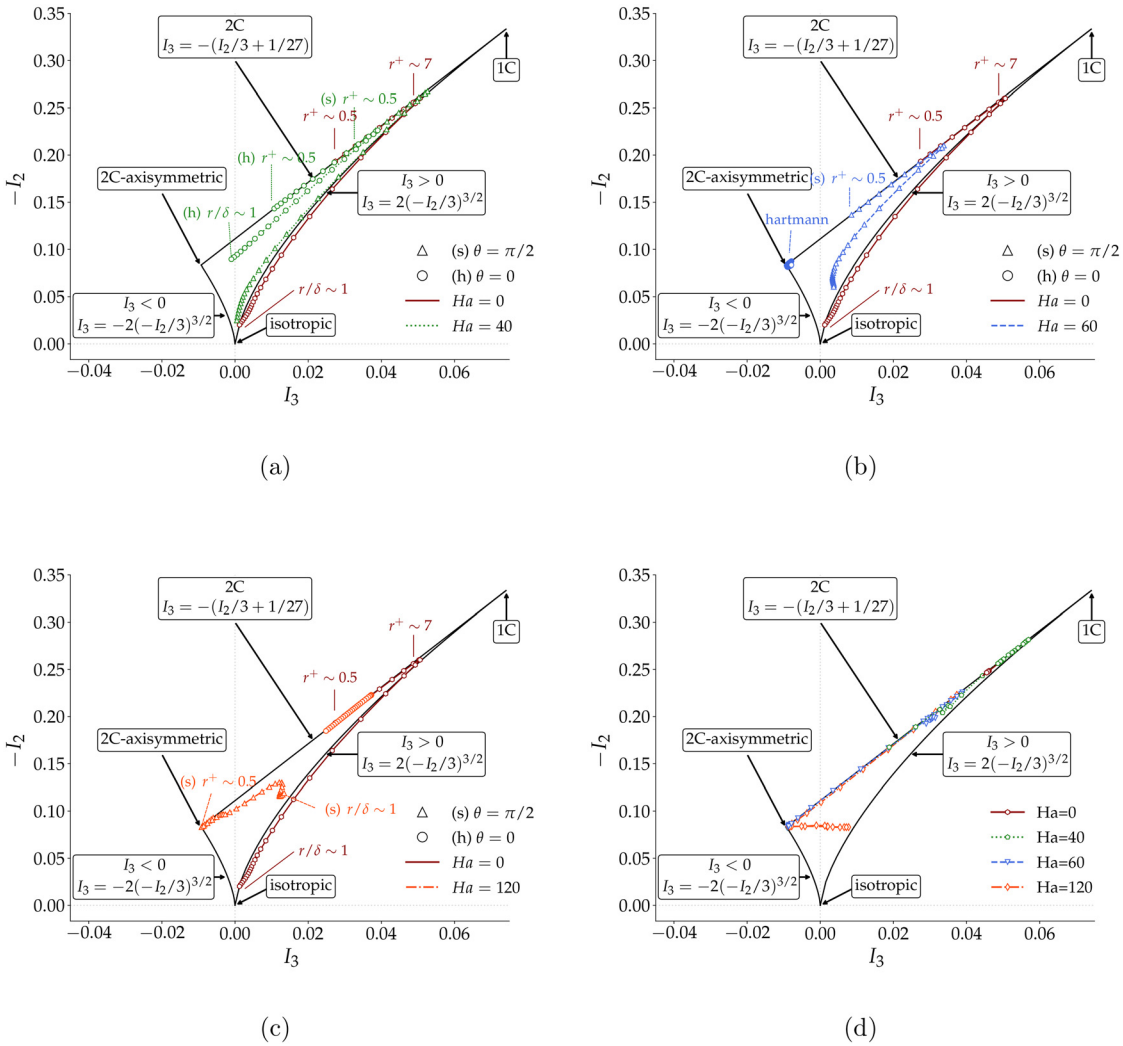

FIG. 22. Anisotropic invariant map on a line going from inner wall to centerline at $\theta = 0$ and $\theta = \pi/2$ [(a)–(c)]. Anisotropic invariant map on circumferential line at $r^+ \simeq 5$ (d).

i.e., showing turbulence appearing in a non-conventional form. This result implies that the magnetic field is able to arrest the mechanism of near-wall streaks formation on the regions parallel to its direction, in addition to a redistribution of turbulent energy from axial and radial to the azimuthal direction component, which in turn seems to be related to the appearance of quasi 2D turbulent states. These states, however, do not permeate the entire domain but are alternated with 3D states depending on the circumferential position.

IV. CONCLUSIONS

A conductive fluid flowing in a uniformly heated annulus within a transversal magnetic field has been simulated with the combined LES/thermal DNS strategy. The magnetic field effects and the heat transfer characteristics have been examined at $Pr = 0.026$ and $Re = 8900$. The Re/Ha ratio was varied from $Re/Ha = 222.5$ to $Re/Ha = 74$, showing a clear modification of the coherent turbulent structures. When the magnetic field is applied, the typical asymmetry of the non-magnetic annulus mean statistics is broken, and the flow characteristics become highly dependent on the circumferential location, i.e., the local orientation between magnetic field and velocity. Indeed, contrarily to the non-magnetic case, the inner wall provides more turbulent kinetic energy compared to the outer wall, because turbulence suppression is larger on the outer wall. The wall friction decreases as a result of suppressed turbulence, but also increases as an indirect effect of a thinner boundary layer (Hartmann effect). In decreasing the Re/Ha ratio, the turbulence suppression contribution is outweighed by the Hartmann effect that tends to be dominant.

The well-resolved temperature field of the LES shows that turbulence suppression has no significant influence on heat transfer and that the temperature field is only influenced due to the modification of the velocity profile. Moreover, the main findings of this work show that at relatively low Re/Ha ratio (in this study, 148 and 74), at least two features can be observed within this geometry:

- The turbulent kinetic energy is partially redistributed by the magnetic field to the azimuthal component, as shown by the investigation of the Reynolds stress tensor 1D power spectra;
- Presence of coexisting quasi-2D and 3D turbulence states in the same flow, depending on the circumferential position.

Overall, this study highlights that less conventional geometries can exhibit a complex interaction of turbulence and magnetic field. This implies that common modeling strategies in low-order approaches may not be adequate for the prediction of the MHD physics and need to be improved, before employing them in engineering design cycles. Finally, this study is limited to electrically insulated walls and forced convection. The wall electrical conductivity can further modify the Lorentz force distribution, that as a consequence, will affect the flow. Large temperature changes can instead set buoyancy motion, coupling the temperature and velocity fields. Therefore, further studies on this subject should also address the effects of wall conductivity parameter and buoyancy.

ACKNOWLEDGMENTS

The authors acknowledge the funding support from Engineering and Physical Science Research Council (EPSRC) under Grant No. EP/R513088/1 and UK Atomic Energy Authority (UKAEA). The authors are grateful for the use of Lovelace HPC at Loughborough University, Sulis Tier-2 at HPC Midlands^{+}, and UK's national facility ARCHER2 via the UK Turbulence Consortium (Grant No. EP/R029326/1).

AUTHOR DECLARATIONS

Conflict of Interest

The authors have no conflicts to disclose.

Author Contributions

Francesco Fico: Conceptualization (equal); Formal analysis (lead); Investigation (lead); Methodology (equal); Software (lead); Visualization (lead); Writing – original draft (lead); Writing – review & editing (equal). **Ivan Langella:** Conceptualization (equal); Funding acquisition (lead); Methodology (equal); Supervision (equal); Writing – review & editing (equal). **Hao Xia:** Conceptualization (equal); Methodology (equal); Project administration (lead); Supervision (equal); Writing – review & editing (equal).

DATA AVAILABILITY

The data that support the findings of this study are available from the corresponding author upon reasonable request.

NOMENCLATURE

b_{ij}	normalized turbulence anisotropic tensor
B	magnetic field
C_f	skin friction coefficient
DNS	direct numerical simulation
$\bar{g}_{ij}$	resolved velocity gradient tensor
Ha	Hartmann number
J	electric current density
k	turbulent kinetic energy
ℓ_F	Lorentz force
LES	large eddy simulation
MHD	magnetohydrodynamic
N	interaction number
p	pressure
Pr	Prandlt number
Q2D	quasi-two-dimensional
r.m.s.	root mean squared
Re	Reynolds number
Re_m	Reynolds magnetic number
R_i, R_0	inner and outer radius
SGS	subgrid scale
S_{ij}	strain rate tensor
$\mathcal{S}^d_{ij}$	traceless symmetric part of the square of velocity gradient tensor
t	time
T_f	friction temperature
T_{ref}	reference temperature
u_x, u_r, u_θ	fluid velocity
WALE	wall-adaptive local eddy viscosity
(x, r, θ)	cylindrical coordinates

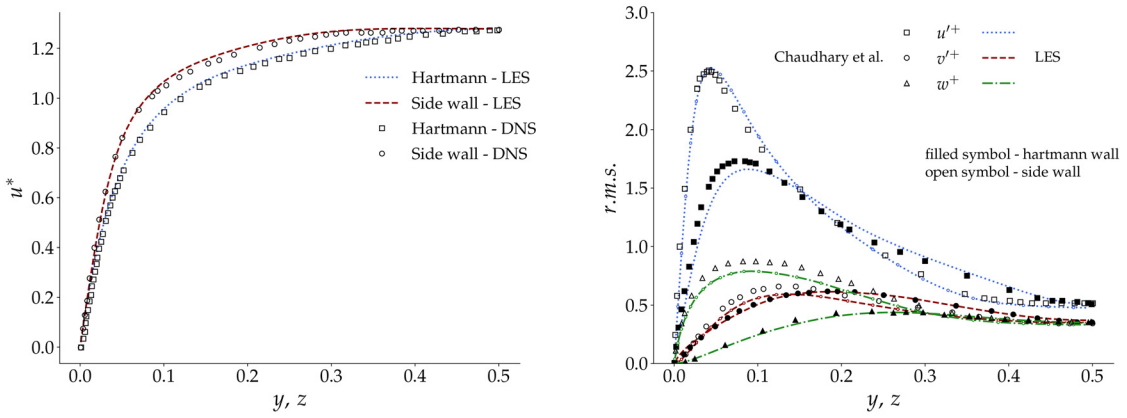

FIG. 23. Mean axial velocity (a) and r.m.s. of velocity fluctuation components (b) for a square duct. Comparison with Chaudhary *et al.*[29]

$\langle\cdot\rangle$	averaged quantity
$\bar{(\cdot)}$	filtered quantity
$(\cdot)'$	fluctuations
$(\cdot)^+$	normalized quantity
α	thermal diffusivity
δ	half walls distance
δ_b	boundary layer thickness
δ_{ij}	Kronecker delta
Δ	cube root of the local cell volume
ε	turbulent dissipation rate
ϵ_{ijk}	Levi–Civita tensor
η, η_T	Kolmogorov and Obukhov–Corrsin scales
Θ	modified temperature
κ	wave number
μ	dynamic viscosity
μ_m	magnetic permeability
ρ	density
σ	electrical conductivity
τ_l	temporal scale
τ_{ij}^{sgs}	subgrid-scale stress tensor
ϕ	electric potential
χ	molecular heat flux

APPENDIX: VALIDATION OF MHD SOLVER

The LES MHD approach has been validated against the DNS data of Chaudhary *et al.*[29] performed on a square duct. The case here reported is at $\mathrm{Re} = 5606$ and $\mathrm{Ha} = 21.2$ (insulated walls). The magnetic field is oriented in the positive y direction. The mesh is uniform in the x (axial) direction, while non-uniform distribution is used for y and z directions. At the walls, the mesh refinement is $\Delta y^+_{wall} \approx \Delta z^+_{wall} \approx 0.4$. While in the core, $\Delta y^+_{core} \approx \Delta z^+_{core} = 5$. The axial resolution is $\Delta x^+ \approx 10$. The mean axial velocity and the r.m.s. of velocity fluctuation components are presented in Figs. 23(a) and 23(b). Both quantities are plotted on the horizontal and vertical bisectors, and streamwise averaged. The mean axial velocity is normalized with the bulk velocity, while the r.m.s. of velocity fluctuation components with the local (on the respective bisector) streamwise averaged friction velocity. The results show very good agreement with DNS data, as can be observed from the figures. The maximum deviation is of 4%, on the transverse r.m.s. of velocity fluctuation component along the sidewall.

REFERENCES

[1] J. A. Brighton and J. B. Jones, "Fully developed turbulent flow in annuli," J. Basic Eng. **86**, 835–842 (1964).
[2] A. Quarmby, "An experimental study of turbulent flow through concentric annuli," Int. J. Mech. Sci. **9**, 205–221 (1967).
[3] K. Rehme, "Turbulence measurements in smooth concentric annuli with small radius ratios," J. Fluid Mech. **72**, 189–206 (1975).
[4] J. M. Nouri, H. Umur, and J. H. Whitelaw, "Flow of Newtonian and non-Newtonian fluids in concentric and eccentric annuli," J. Fluid Mech. **253**, 617 (1993).
[5] S. Y. Chung, G. H. Rhee, and H. J. Sung, "Direct numerical simulation of turbulent concentric annular pipe flow," Int. J. Heat Fluid Flow **23**, 426–440 (2002).
[6] B. J. Boersma and W.-P. Breugem, "Numerical simulation of turbulent flow in concentric annuli," Flow Turbul. Combust. **86**, 113–127 (2010).
[7] E. Bagheri, B.-C. Wang, and Z. Yang, "Influence of domain size on direct numerical simulation of turbulent flow in a moderately curved concentric annular pipe," Phys. Fluids **32**, 065105 (2020).
[8] S. Y. Chung and H. J. Sung, "Direct numerical simulation of turbulent concentric annular pipe flow," Int. J. Heat Fluid Flow **24**, 399–411 (2003).
[9] E. Bagheri and B.-C. Wang, "Direct numerical simulation of turbulent heat transfer in concentric annular pipe flows," Phys. Fluids **33**, 055131 (2021).
[10] S. Malang and R. Mattas, "Comparison of lithium and the eutectic lead-lithium alloy, two candidate liquid metal breeder materials for self-cooled blankets," Fusion Eng. Des. **27**, 399–406 (1995).
[11] G. Federici, R. Kemp, D. Ward, C. Bachmann, T. Franke, S. Gonzalez, C. Lowry, M. Gadomska, J. Harman, B. Meszaros, C. Morlock, F. Romanelli, and R. Wenninger, "Overview of EU DEMO design and R&D activities," Fusion Eng. Des. **89**, 882–889 (2014).
[12] F. Roelofs, "Liquid metal thermal hydraulics: State-of-the-art and future perspectives," Nucl. Eng. Des. **362**, 110590 (2020).
[13] G. Grötzbach, "Challenges in low-Prandtl number heat transfer simulation and modelling," Nucl. Eng. Des. **264**, 41–55 (2013).
[14] G. Grötzbach, "Revisiting the resolution requirements for turbulence simulations in nuclear heat transfer," Nucl. Eng. Des. **241**, 4379–4390 (2011).

[15]L. Bricteux, M. Duponcheel, G. Winckelmans, I. Tiselj, and Y. Bartosiewicz, "Direct and large eddy simulation of turbulent heat transfer at very low Prandtl number: Application to lead–bismuth flows," Nucl. Eng. Des. **246**, 91–97 (2012).
[16]L. Marocco, "Hybrid LES/DNS of turbulent forced and aided mixed convection to a liquid metal flowing in a vertical concentric annulus," Int. J. Heat Mass Transfer **121**, 488–502 (2018).
[17]Y. Bartosiewicz and M. Duponcheel, "Large-eddy simulation: Application to liquid metal fluid flow and heat transfer," *Thermal Hydraulics Aspects of Liquid Metal Cooled Nuclear Reactors* (Woodhead Publishing, 2019), pp. 245–271.
[18]L. Marocco and F. Garita, "Large eddy simulation of liquid metal turbulent mixed convection in a vertical concentric annulus," J. Heat Transfer **140**, 072504 (2018).
[19]B. Lehnert, "The decay of magneto-turbulence in the presence of a magnetic field and Coriolis force," Q. Appl. Math. **12**, 321–341 (1955).
[20]H. K. Moffatt, "On the suppression of turbulence by a uniform magnetic field," J. Fluid Mech. **28**, 571 (1967).
[21]J. Hartmann and F. Lazarus, "Hg-dynamics. II. Experimental investigations on the flow of mercury in a homogeneous magnetic field," K. Dan. Vidensk. Selsk. Mat. Fys. Medd. **15**, 7 (1937).
[22]R. A. Gardner and P. S. Lykoudis, "Magneto-fluid-mechanic pipe flow in a transverse magnetic field. I. Isothermal flow," J. Fluid Mech. **47**, 737–764 (1971).
[23]D. Lee and H. Choi, "Magnetohydrodynamic turbulent flow in a channel at low magnetic Reynolds number," J. Fluid Mech. **439**, 367–394 (2001).
[24]S. Satake, T. Kunugi, and S. Smolentsev, "Direct numerical simulations of turbulent pipe flow in a transverse magnetic field," J. Turbul. **3**, N20 (2002).
[25]D. Krasnov, O. Zikanov, J. Schumacher, and T. Boeck, "Magnetohydrodynamic turbulence in a channel with spanwise magnetic field," Phys. Fluids **20**, 095105 (2008).
[26]P. Burattini, O. Zikanov, and B. Knaepen, "Decay of magnetohydrodynamic turbulence at low magnetic Reynolds number," J. Fluid Mech. **657**, 502–538 (2010).
[27]A. Alemany, R. Moreau, P. L. Sulem, and U. Frisch, "Influence of an external magnetic field on homogeneous MHD turbulence," J. Mec. **18**, 277–313 (1979).
[28]P. A. Davidson, "The role of angular momentum in the magnetic damping of turbulence," J. Fluid Mech. **336**, 123–150 (1997).
[29]R. Chaudhary, S. P. Vanka, and B. G. Thomas, "Direct numerical simulations of magnetic field effects on turbulent flow in a square duct," Phys. Fluids **22**, 075102 (2010).
[30]S. Dong, D. Krasnov, and T. Boeck, "Secondary energy growth and turbulence suppression in conducting channel flow with streamwise magnetic field," Phys. Fluids **24**, 074101 (2012).
[31]O. Zikanov and A. Thess, "Direct numerical simulation of forced MHD turbulence at low magnetic Reynolds number," J. Fluid Mech. **358**, 299–333 (1998).
[32]T. Boeck, D. Krasnov, and E. Zienicke, "Numerical study of turbulent magnetohydrodynamic channel flow," J. Fluid Mech. **572**, 179–188 (2007).
[33]O. Zikanov, D. Krasnov, T. Boeck, and S. Sukoriansky, "Decay of turbulence in a liquid metal duct flow with transverse magnetic field," J. Fluid Mech. **867**, 661–690 (2019).
[34]S. Smolentsev, "Physical background, computations and practical issues of the magnetohydrodynamic pressure drop in a fusion liquid metal blanket," Fluids **6**, 110 (2021).
[35]S. Satake, T. Kunugi, K. Takase, and Y. Ose, "Direct numerical simulation of turbulent channel flow under a uniform magnetic field for large-scale structures at high Reynolds number," Phys. Fluids **18**, 125106 (2006).
[36]A. Pothérat and K. Kornet, "The decay of wall-bounded MHD turbulence at low," J. Fluid Mech. **783**, 605–636 (2015).
[37]H. Kobayashi, "Large eddy simulation of magnetohydrodynamic turbulent duct flows," Phys. Fluids **20**, 015102 (2008).
[38]D. Krasnov, O. Zikanov, and T. Boeck, "Numerical study of magnetohydrodynamic duct flow at high Reynolds and Hartmann numbers," J. Fluid Mech. **704**, 421–446 (2012).
[39]A. Rasam and Z. Pouransari, "Numerical investigation of the Lorentz force effect on two-point statistics in a turbulent channel flow," Phys. Fluids **32**, 115112 (2020).
[40]J. Sommeria and R. Moreau, "Why, how, and when, MHD turbulence becomes two-dimensional," J. Fluid Mech. **118**, 507 (1982).
[41]B. Knaepen and R. Moreau, "Magnetohydrodynamic turbulence at low magnetic Reynolds number," Annu. Rev. Fluid Mech. **40**, 25–45 (2008).
[42]O. Zikanov, D. Krasnov, T. Boeck, A. Thess, and M. Rossi, "Laminar-turbulent transition in magnetohydrodynamic duct, pipe, and channel flows," ASME Appl. Mech. Rev. **66**, 030802 (2014).
[43]S. Smolentsev, R. Moreau, L. Bühler, and C. Mistrangelo, "MHD thermofluid issues of liquid-metal blankets: Phenomena and advances," Fusion Eng. Des. **85**, 1196–1205 (2010).
[44]K. Ma and J. Liu, "Liquid metal cooling in thermal management of computer chips," Front. Energy Power Eng. China **1**, 384–402 (2007).
[45]M. Sheikholeslami, M. Gorji-Bandpay, and D. Ganji, "Magnetic field effects on natural convection around a horizontal circular cylinder inside a square enclosure filled with nanofluid," Int. Commun. Heat Mass Transfer **39**, 978–986 (2012).
[46]K. Morita, W. Maschek, M. Flad, H. Yamano, and Y. Tobita, "Thermophysical properties of lead-bismuth eutectic alloy in reactor safety analyses," J. Nucl. Sci. Technol. **43**, 526–536 (2006).
[47]S. Patankar, C. Liu, and E. Sparrow, "The periodic thermally developed regime in ducts with streamwise periodic wall temperature or heat flux," Int. J. Heat Mass Transfer **21**, 557–566 (1978).
[48]X. Fang and B.-C. Wang, "On the turbulent heat transfer in a square duct subjected to spanwise system rotation," Int. J. Heat Fluid Flow **71**, 220–230 (2018).
[49]P. A. Davidson, *An Introduction to Magnetohydrodynamics* (Cambridge University Press, Cambridge, New York, 2001).
[50]F. Nicoud and F. Ducros, "Subgrid-scale stress modelling based on the square of the velocity gradient tensor," Flow Turbul. Combust. **62**, 183–200 (1999).
[51]H. G. Weller, G. Tabor, H. Jasak, and C. Fureby, "A tensorial approach to computational continuum mechanics using object-oriented techniques," Comput. Phys. **12**, 620 (1998).
[52]R. Issa, "Solution of the implicitly discretised fluid flow equations by operator-splitting," J. Comput. Phys. **62**, 40–65 (1986).
[53]S. V. Patankar, *Numerical Heat Transfer and Fluid Flow* (CRC Press, 1980).
[54]M.-J. Ni, R. Munipalli, P. Huang, N. B. Morley, and M. A. Abdou, "A current density conservative scheme for incompressible MHD flows at a low magnetic Reynolds number. I. On a rectangular collocated grid system," J. Comput. Phys. **227**, 205–228 (2007).
[55]S. B. Pope, *Turbulent Flows* (Cambridge University Press, Cambridge, New York, 2000).
[56]R. J. Moreau, *Magnetohydrodynamics* (Springer, The Netherlands, 1990).
[57]A. Blishchik and S. Kenjereš, "Turbulence suppression and regeneration in a magnetohydrodynamic duct flow due to influence of arbitrary electrically conductive walls," Phys. Fluids **34**, 045101 (2022).
[58]S. I. Chernyshenko and M. F. Baig, "The mechanism of streak formation in near-wall turbulence," J. Fluid Mech. **544**, 99 (2005).
[59]P. A. Davidson, *Turbulence: An Introduction for Scientists and Engineers* (Oxford University Press, 2015).
[60]J. L. Lumley, "Computational modeling of turbulent flows," *Advances in Applied Mechanics* (Elsevier, 1979), pp. 123–176.
[61]A. J. Simonsen and P.-Å. Krogstad, "Turbulent stress invariant analysis: Clarification of existing terminology," Phys. Fluids **17**, 088103 (2005).
[62]P.-Å. Krogstad and L. E. Torbergsen, "Invariant analysis of turbulent pipe flow," Flow Turbul. Combust. **64**, 161–181 (2000).